High-Energy-Density Waterborne Dielectrics from Polyelectrolyte-Colloid Complexes

Junjin Che, Cécile Zakri, Isabelle Ly, Wilfrid Neri, Eric Laurichesse, Jean-paul Chapel, Philippe Poulin, Jinkai Yuan

To cite this version:

Junjin Che, Cécile Zakri, Isabelle Ly, Wilfrid Neri, Eric Laurichesse, et al.. High-Energy-Density Waterborne Dielectrics from Polyelectrolyte-Colloid Complexes. Advanced Functional Materials, In press, pp.2213804. ⟨10.1002/adfm.202213804⟩. ⟨hal-04044230⟩

HAL Id: hal-04044230
https://hal.science/hal-04044230v1

Submitted on 24 Mar 2023

High-Energy-Density Waterborne Dielectrics from Polyelectrolyte-Colloid Complexes

*Junjin Che, Cécile Zakri, Isabelle Ly, Wilfrid Neri, Eric Laurichesse, Jean-Paul Chapel, Philippe Poulin, Jinkai Yuan**

Dr. J. Che, Prof. C. Zakri, I. Ly, W. Neri, E. Laurichesse, Dr. J.-P. Chapel, Dr. P. Poulin, Dr. J. Yuan
Centre de Recherche Paul Pascal, CNRS
Université de Bordeaux
UMR 5031, 33600 Pessac, France
E-mail: jinkai.yuan@crpp.cnrs.fr (J.Y.)

Abstract

To meet the demands of miniaturization and integration of next-generation power systems, a major challenge is to improve the energy density of used dielectric capacitors. Polymers based nanocomposites are of great potential for high-energy-density capacitors. However, most of them are prepared via melt blending at high temperatures or solution processing in hazardous organic solvents, which are energy consuming and environmentally problematic. It has long remained challenging to develop new dielectric materials economically and ecologically. Here, we report a class of high-energy-density dielectrics made by electrostatically complexing low-cost PVDF latex with oppositely charged chitosan in an aqueous phase. It is found that, at the charge neutralization point, the film of PVDF@Chitosan complexes demonstrates the highest breakdown strength (630 MV m^{-1}) and recoverable energy density (10.1 J cm^{-3}), which are respectively 279% and 421% higher than the bare PVDF latex film, and far beyond most of the conventional solvent- or melt-processed polymer films. The largely improved capacitive performances are ascribed to the significant minimization of losses at the critical charge neutralization point. The concept can be extended to a wide range of colloids, including polystyrene latex and aqueous bentonite suspension, highlighting the versatility of the proposed approach to develop environmentally friendly high-performance capacitors.

1. Introduction

Dielectric materials are capable of storing energy in the form of electric displacement upon application of an electric field. This energy storage mechanism endows them an intrinsic fast energy uptake and delivery with times ranging from nanoseconds to milliseconds.[1] The electrostatic capacitors based on dielectric materials are increasingly pervasive in modern electronics and pulsed power systems.[2-5] Nevertheless, capacitors generally have lower energy densities compared with other electrochemical energy storage systems such as batteries.[6] Today, many of the advanced electronic and electrical systems require high integration, compactness, and miniaturization, leading to the rapid development of new dielectrics that have high energy density and high efficiency.[7-10]

The energy built up in dielectric materials is determined by the applied electric field E and the consequent dielectric polarization P. The maximum stored energy density U_{s} is expressed as $\int_0^{P_m} EdP$, where P_{m} is the maximum polarization.[11] Yet only a portion of the stored energy can be effectively discharged due to the existence of hysteresis losses, leading to a remnant polarization, P_{r}. The discharged energy density U_{d} can then be calculated as $\int_{P_r}^{P_m} EdP$ (Figure S1, Supporting Information).[12] The energy storage efficiency is defined as $U_{\mathrm{d}}/U_{\mathrm{s}}$. Thus, a combination of large polarization variation (P_{m}-P_{r}) and high breakdown strength E_{b} is highly desired to achieve a high U_{d}.[13]

Conventional dielectric materials are ceramics with large spontaneous polarization and excellent thermal stability.[14] Yet they suffer from low breakdown strength and challenging processing conditions.[15] As alternatives, polymers have facile processability, high breakdown strength, and low energy losses.[10, 16, 17] However, their low permittivity (k<10) poses a critical challenge for the technological implementation in miniaturized devices. Due to the inverse correlation between the polarization and breakdown strength ($E_b = k^{-0.65}$),[18] the achieved U_d to date is still limited (<5 J cm^{-3}) for capacitors based on ceramics or polymers alone.[2] Some strategies have emerged to further enhance U_d via developing polymer nanocomposites with disparate components/phases, such as designing novel morphology of hybrid fillers,[19-21] modulating macromolecular organizations,[16, 22-24] creating multilayered structures,[11, 25-30] and establishing dielectric anisotropy.[31-34] So far, most of existing polymer nanocomposites are prepared via melt blending at high temperatures or solution processing in hazardous organic solvents, which are energy consuming and environmentally problematic. It has long remained challenging to develop new dielectric materials economically and ecologically.

Herein, we target high-energy dielectric materials by colloidal engineering in aqueous phase. Colloids have been used as building blocks to construct diverse functional materials with emergent physical properties,[35] such as proton conductive membranes,[36] plasmonic nanostructures,[37] organic photovoltaic devices,[38, 39] and field-effect transistors.[40] Generally, water-based colloids are electrostatically stabilized by surface charges. The high density of charges on the particle surface create conductive paths. These highly conductive domains induce significant leakage and dramatically reduce the breakdown strength of the solidified material. To the best of our knowledge, water-processable colloid based dielectrics are lacking until now. In this work, we propose to electrostatically complex colloids with oppositely charged polyelectrolyte to neutralize their surface charges and develop waterborne high-energy dielectrics.

2. Results and Discussion

We start from water-based polyvinylidene fluoride (PVDF) latex with low cost, environmental friendliness, and particularly the known high permittivity. The PVDF latex dispersion can remain as individual particles for an appreciable time (Figure 1a). Such electrostatic stabilization arises from the dissociation of the carboxylic groups on the latex nanoparticles. Protonated chitosan (NH_3^+), a biosourced water-soluble polymer, is chosen as a cationic polyelectrolyte to electrostatically interact with latex nanoparticles and to finely tune the charge neutralization of generated hybrid particles. The PVDF@Chitosan hybrid dispersions display distinct scenarios depending on the fraction of chitosan f_{Chitosan} (Figure 1a).

At low f_{Chitosan} up to 0.3%, stable PVDF latex particles are partially decorated with chitosan chains, generating individual hybrid particles with a net negative charge (*zeta* potential<-43 mV, Figure 1b, c; Table S1, Supporting Information). By increasing the fraction up to 0.6%, the negative surface charges carried by the PVDF latex particles are progressively compensated by the cationic groups (NH_3^+) present on the chitosan chains and by the decreased pH. But the amplitude of the *zeta* potential still remains above 30 mV, a critical value, above which a colloidal suspension is considered to be electrostatically stabilized.[41] However, the size of the complexes increases by an order of magnitude (Table S1, Supporting Information), suggesting that bridging between the latex particles by the chitosan chains is the dominant mechanism involved at this stage. Such bridging is a consequence of the adsorption of the segments of individual chitosan chain onto the surfaces of more than one PVDF particle (Figure 1b). In the vicinity of 0.8%, the hybrid particles become significantly less charged, and are then subject to increasing hydrophobic interactions. The dispersion becomes unstable with the formation of loose and jammed assemblies as a result of the Brownian collisions of hybrid particles. Near this point, bridging may still be operational, but the mass ratio corresponds quite closely to the dosage of chitosan required to neutralize the surface charge of the PVDF particles. Such charge neutralization is experimentally revealed by the reduction of the measured electrophoretic mobility of the particles to nearly zero (the isoelectric point, Figure 1c), the pH down to 7 (Table S1, Supporting Information), and the increase of colloid size to the largest value (~6.5 μm, Figure 1c). At higher fractions beyond 1%, a net charge reversal occurs due to the macromolecular nature of the chitosan chains, yielding more charged and stable cationic hybrid particles with much smaller sizes (Figure 1c). The *zeta* potential then becomes more and more positive with values above +30 mV, promoting a very stable dispersion. At this stage, steric and electrosteric stabilization start to take place.[41]

The complexation of PVDF and chitosan screens their Coulombic attraction with respective counterions. In particular, at the isoelectric point (0.8 %), all charged latex particles and chitosan chains presumably engage in the formation of complexes through ion-pairing, promoting a complete liquid-solid phase separation with the release of all counterions into the supernatant phase. This mechanism is highly analogous to the widespread associative process of oppositely charged polyelectrolytes in aqueous solutions.[42] Intriguingly, the charge-neutralized PVDF@Chitosan complexes are film forming under infrared light, yielding freestanding waterborne films, showing a segregated nanostructure with a clear boundary between the PVDF nanoparticles (Figure 1d). Indeed, the chitosan chains wrapped around the PVDF nanoparticles prevent their coalescence. The resulting hybrid and segregated nanostructure is extremely stable and can be maintained even after hot pressing at 110°C. Actually, chitosan has excellent film-forming properties. Not only does it drive the assembly of PVDF latex particles, but it also fills the voids or cracks that usually form when water evaporates from the colloidal dispersion. Figure 1e shows a photograph of a freestanding PVDF@Chitosan dielectric film. The patterned latex films are typically ~10 µm thick and are highly uniform, flexible, and crack-free.

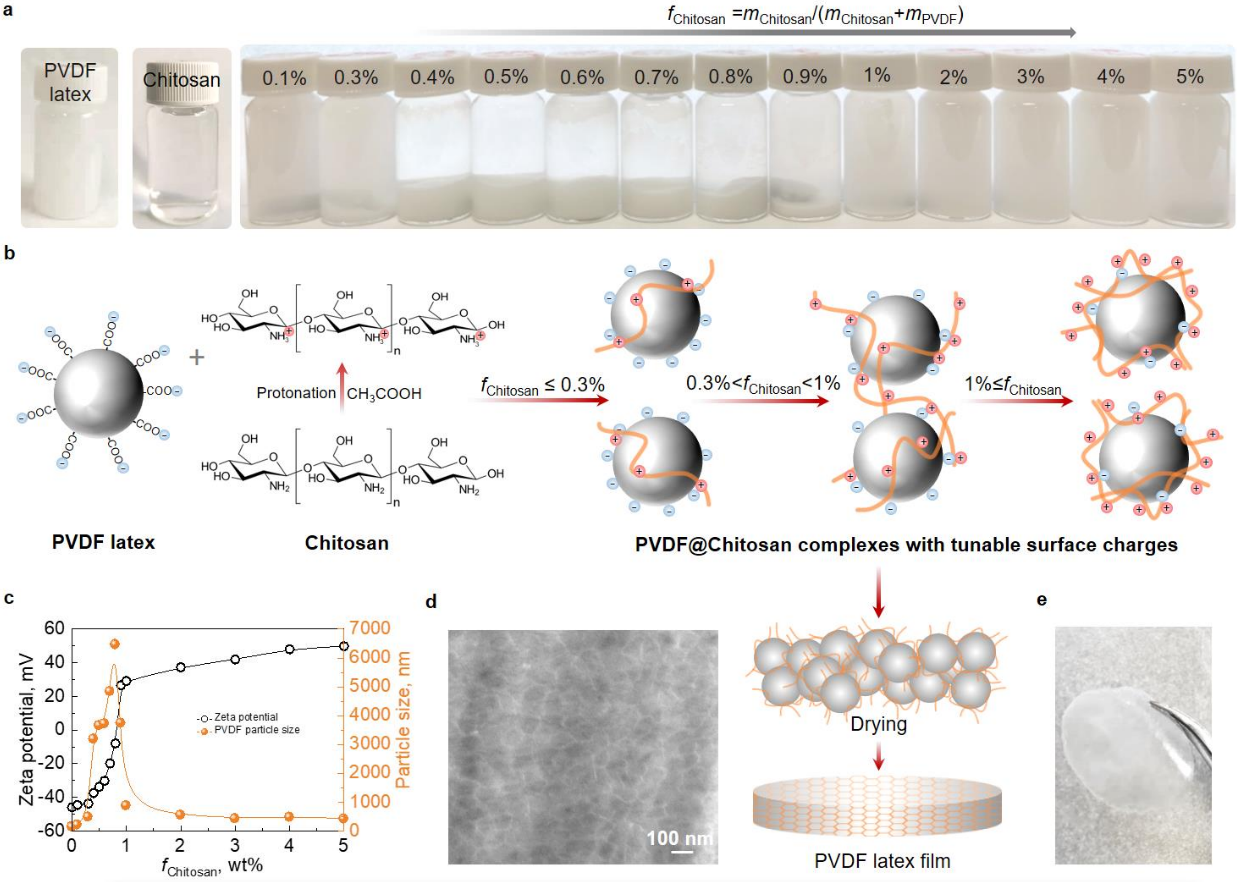

Figure 1. PVDF@Chitosan complexes and waterborne dielectric films. a) Photographs of PVDF latex dispersion (0.72 wt%), aqueous chitosan solution (0.66 wt%), and their mixtures at different mass ratios. b) Schematic illustrations of the electrostatic interactions between negatively charged PVDF particles and cationic chitosan chains at different stages of mass ratios. By increasing the $f_{Chitosan}$, the pH of dispersions decreases, the latex particles and chitosan macromolecules become less and more charged respectively. c), *Zeta* potential of the different dispersions as well as the size of the PVDF@Chitosan complexes as a function of the mass ratio. d) TEM image, e) photograph of a free-standing waterborne PVDF@Chitosan dielectric film with a $f_{Chitosan}$ of 0.8%.

To confirm the potential dielectric applications of PVDF@Chitosan complex films, we examine their structural, mechanical and dielectric properties and compare them with coalesced PVDF latex films. Figure 2a schematizes the formation of pure PVDF latex films. As the water evaporates, the uniformly and stably dispersed bare PVDF particles come into contact with each other. When PVDF latex particles have reached their maximum packing, compression and coalescence of the particles begin towards the formation of a continuous film. Additional thermal annealing is used to remove defects, remaining voids or cracks after the film has solidified. The cross-sectional scanning electron microscope (SEM) images confirm the coalescence of PVDF nanoparticles into a continuous single phase (Figure 2b, c). On the other hand, the PVDF@Chitosan system, due to the bridging and compensation of positive and negative charges, undergoes a liquid-solid phase separation, eventually leading to gravity sedimentation over time (Figure 2d). After removing the supernatant, the sediment is readily cast into thin films. Due to the existence of chitosan coating on the surface of PVDF nanoparticles, they are not able to fully contact each other. The presence of chitosan chains ultimately prevents the complete coalescence of PVDF nanoparticles yet promotes the self-assembly of PVDF nanoparticles into a closely packed heterogeneous film (Figure 2e, f). Such unique heterogeneous structure is further evidenced by the elemental distribution maps of the PVDF@Chitosan film. (Figure S2, Supporting Information).

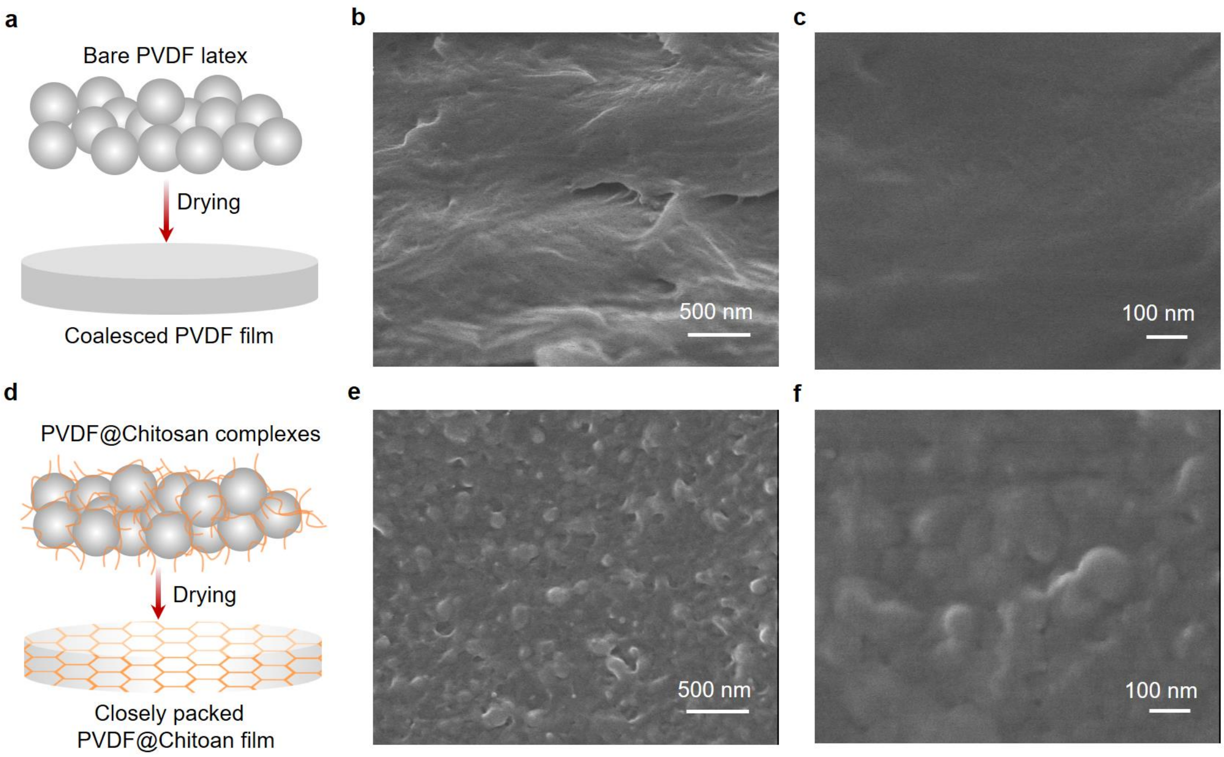

Figure 2. a) Schematic illustration of the inner structure of the coalesced latex films. b,c) SEM images under different magnifications of a cross-sectional PVDF latex film, which is directly cast from the latex dispersion, followed by hot-pressing at 110 °C. d) Schematics of the heterogeneous structure of PVDF@Chitosan film. e,f) The cross-sectional SEM images of PVDF@Chitosan film, which is derived from a mixture dispersion with a f_{Chitosan} of 0.8%, followed by incubation under infrared light and subsequent hot pressing at 110 °C.

The tensile properties of coalesced PVDF films and PVDF@Chitosan complex films have been characterized and compared with typical solvent-processed PVDF polymers. Latex films display mechanical properties distinct from conventional PVDF films (Figure 3). They are not as stiff as the latter, exhibiting lower Young's moduli. However, latex films can withstand a large plastic deformation (~820%) before break, which is 64 times higher than that of typical PVDF film. Such mechanical behaviors are highly akin to thermoplastic elastomers.[43] Furthermore, as compared to the coalesced PVDF film, Young's modulus of PVDF@Chitosan film decreases by 50%, yet the elongation at break and ultimate tensile strength decline only by 7% and 10% respectively. In essence, the non-coalesced PVDF@Chitosan films basically retain the tensile mechanical strength of latex particles.

Generally, polymer films experience a large compressive stress under a high electric field applied along the out-of-plane direction. One can estimate the greatest compressive strain for the weakest materials under study, which is PVDF@Chitosan film with Young's modulus of 16 MPa. The compressive strain is defined as $\frac{t_0}{t}$, where t and t_0 are the thickness of the films with and without electric field. This strain is given by equating the electrical stress generated by the field to the mechanical stress of the polymer, and can be calculated by $\varepsilon_0 \varepsilon_r E^2 = Y ln\left(\frac{t_0}{t}\right)$, where E is the applied electric field and Y the Young's modulus of the polymer. A logarithmic form of compressive stress is used to account for the large deformation level at high fields. Considering a field of 200 MV m^{-1}, a permittivity of 10 and Young's modulus of 16 MPa leads to a compressive strain $\frac{t_0}{t}$ of about 1.25. This strain remains well below the critical value of 1.65, above which the thin film would collapse and display an electromechanical instability.[44] Materials with greater Young's modulus are expected to display levels of compressive strains below 1.25. Therefore, our PVDF@Chitosan films are mechanically sound for further dielectric applications.

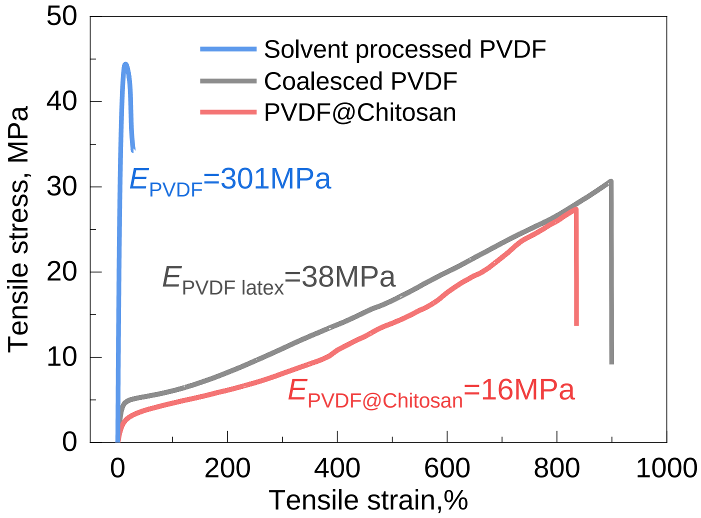

Figure 3. The tensile stress versus tensile strain curves for typical PVDF processed in N, N-dimethylformamide, coalesced PVDF latex film, and PVDF@Chitosan film at $f_{Chitosan}$ of 0.8%. Young's modulus, E, of each film is indicated.

We further performed dielectric characterizations of PVDF latex samples to explore their potential for capacitive energy storage. Figure 4a shows the permittivity of PVDF latex films as a function of frequency and the fraction of chitosan used to neutralize charges of PVDF nanoparticles. The coalesced PVDF latex film displays a drop of apparent permittivity at low frequency. This arises from the polarization of the electrodes as a result of the formation of the electric double layer, in which the charges on the electrodes are balanced by the adsorption of mobile charges present in the latex film. Due to the existence of such mobile charges, the apparent permittivity is higher than solvent- or melt-processed PVDF films (k~10),[45, 46] and accompanied by a relatively large dielectric loss (tanδ>0.1, Figure 4b). The same mechanism is illustrated in ion-containing polyvinyl alcohol (PVA) films (Figure S3, Supporting Information). On the other hand, the permittivity of PVDF@Chitosan films decreases continuously and becomes less frequency-dependent as the level of charge neutralization of hybrid particles increases (Figure 1c, Figure 4a). A similar downward trend is also found for loss tangent. At the critical isoelectric point (0.8%), the material demonstrates the lowest loss (0.05@10 kHz), and exhibits a permittivity of 6. Beyond the isoelectric point, the additional chitosan chains reverse the net charge and promote an increasing charge density on the formed complexes. This in turn gives rise again to large losses and permittivity, as evidenced by the dielectric spectroscopy of PVDF@Chitosan films with elevated f_{Chitosan} ranging from 1 wt% to 5 wt% (Figure S4, Supporting Information).

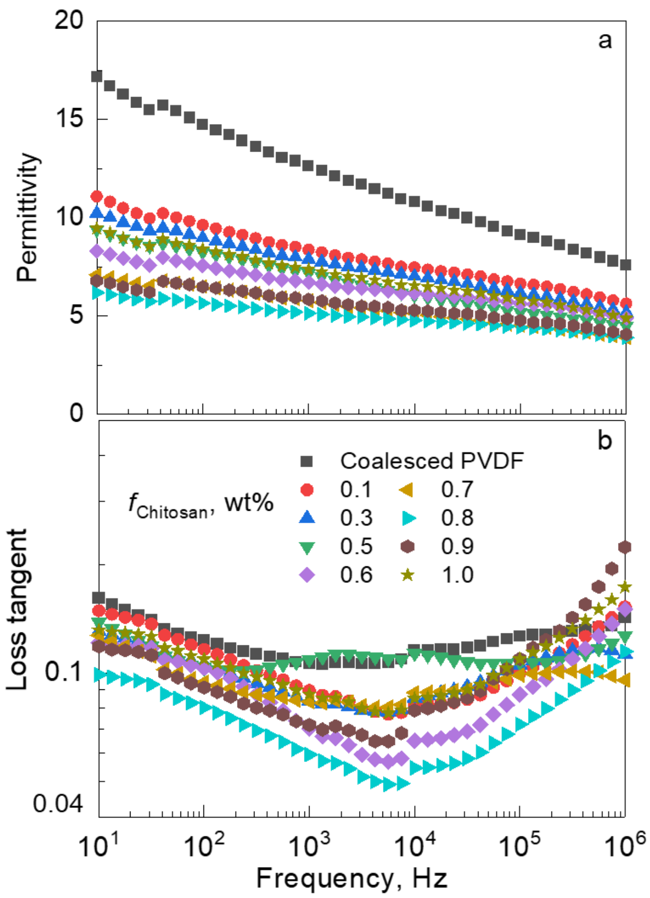

Figure 4. a) Frequency dependence of permittivity for coalesced PVDF latex and PVDF@Chitosan films. b) Loss tangent of coalesced PVDF latex and PVDF@Chitosan films as a function of frequency.

Generally, as compared to solvent- or melt-processed materials, waterborne polymer films tend to contain a relatively larger number of charged species and suffer from lower breakdown strength. However, the improved insulating properties of PVDF@Chitosan films at $f_{Chitosan}$ of 0.8% hold great promise to withstand a high voltage. To confirm this key feature for capacitive energy storage, we recorded the voltages applied incrementally until the dielectric breakdown. The E_b and shape factor β are calculated by a linear fit using the Weibull failure statistics (Figure 5a, Table S2, Supporting Information). E_b of coalesced PVDF latex film is found to be 226 MV m^{-1}, which is much lower than those (from 350 MV m^{-1} to 400 MV m^{-1}) achieved in typical PVDF films via conventional solution casting or melt-extrusion.[45, 47, 48] The reason is the presence of free charge carriers in the waterborne coalesced PVDF latex film. The mobile charges on the particle surfaces migrate easily under a high electric field. They induce Joule heating and make the material susceptible to breakdown. Such effect of mobile ions on E_b has been also verified in solid ion-containing PVA/CH_3COONa films (Figure S5, Supporting Information). However, the introduction of a trace amount of chitosan greatly improves the breakdown strength of PVDF latex films. The E_b of PVDF@Chitosan film continuously increases with chitosan content and reaches a maximum value of 630 MV m^{-1} at the isoelectric point (0.8 wt%), representing an improvement of 179% (Figure 5b). This behavior can be understood by considering the charge compensation process by ion-pairing and the morphology of resulting PVDF@Chitosan films. As they approach the isoelectric point, the negatively charged PVDF nanoparticles are progressively neutralized and linked together via chain bridging and/or hydrophobic interactions. The resultant large assemblies sediment, releasing counterions from the solid phase to the aqueous liquid phase. In this regard, a lower density of charges remain on the surface of PVDF@Chitosan hybrid particles, with which the built film has a higher breakdown strength. In addition, PVDF nanoparticles are wrapped by chitosan chains, which prevent their coalescence and promote their self-assembly into a very compact but heterogeneous film. Such structure is highly favorable to eliminate leakage currents with barriers or traps between polarizable PVDF particles.[49] The formed convoluted paths staunch the initiation and propagation of electrical treeing, leading to high E_b.[34] The neutral charge state of PVDF@Chitosan complexes, together with the heterogeneous nanostructures, contributes to the conspicuous improvement of the breakdown strength. Beyond the isoelectric point, the breakdown strength declines rapidly with the addition of more chitosan chains (Figure 5b, Figure S6, Supporting Information). At this stage, the heterogeneous nanostructure can always remain, but the excessive chitosan promotes an increasing density of dissociated charges located at the particle boundaries and makes the barrier conductive. The formed conductive paths induce leakage and reduce the breakdown strength.

Thanks to the adequately enhanced E_b, a waterborne high-energy dielectric can be envisioned. We characterized the polarization and energy storage density of PVDF@Chitosan films at high electric fields. The polarization-electric field (P-E) hysteresis loops of each film were first measured under an electric field of 200 MV m^{-1}, which is close to the E_b of bare PVDF latex film. With increasing $f_{Chitosan}$, the maximum electric displacement P_m decreases yet the hysteresis loop becomes thinner (reduced P_r), both reaching the limit at 0.8 wt% (Figure 5c). This indicates that the neutralization of PVDF nanoparticles partially loses the polarization capacity related to ion activities in the system but gains a larger portion of the discharged energy. The polarization of fully charge-neutralized PVDF based film is evaluated at fields up to E_b (Figure 5d). P_m-P_r increases with the electric field and reaches the highest value of 36.8 mC m^{-2} at 630 MV m^{-1}. This polarization variation is also superior to the values of pure PVDF latex and other PVDF@Chitosan composite films measured at fields approaching their E_b (Figure S7, Supporting Information). The discharged energy density U_d and efficiency η are calculated from the P-E loops of each film and presented in Figure 5e. Combining the largest P_m-P_r and the highest E_b, the PVDF@Chitosan film at $f_{Chitosan}$ of 0.8% achieves the highest U_d of 10.1 J cm^{-3}, which is 4.2 times higher than bare latex film (U_d=2.4 J cm^{-3}), and more than twice of typical PVDF materials.[47] The high U_d should be ascribed to the low loss (small P_r) and the greatly improved E_b due to the surface charge neutralization and the formed heterogeneous nanostructure. In addition, the η at the isoelectric point (0.8%) is higher than its counterparts at each field, and maintains high values (>~72%) as the electric fields approach E_b. The high efficiency is associated with the suppressed leakage current in the charge-neutralized system. Above the isoelectric point, excessive chitosan (from 0.9 wt% to 5 wt%), however, lead to a degraded energy storage performance due to the reduced E_b and increased conduction losses, both of which lead to a striking decline in U_d and η (Figure S8, Supporting Information).

Figure 5f compares the U_d and η values of our charge-neutralized PVDF film with those of recently reported high-energy-density polymer-based dielectrics, including all-organic polymers,[22, 50-60] and inorganic/organic nanocomposites.[3, 61] Indeed, our charge-neutralized PVDF film exhibits concurrently high U_d and η. In addition, most polymer dielectrics are either melt-extruded at high temperatures or processed in hazardous organic solvents. Their manufacturing process is, therefore, not economical and ecological. Our strategy based on soft-chemistry processes holds great potential for environmentally friendly high-performance capacitors.

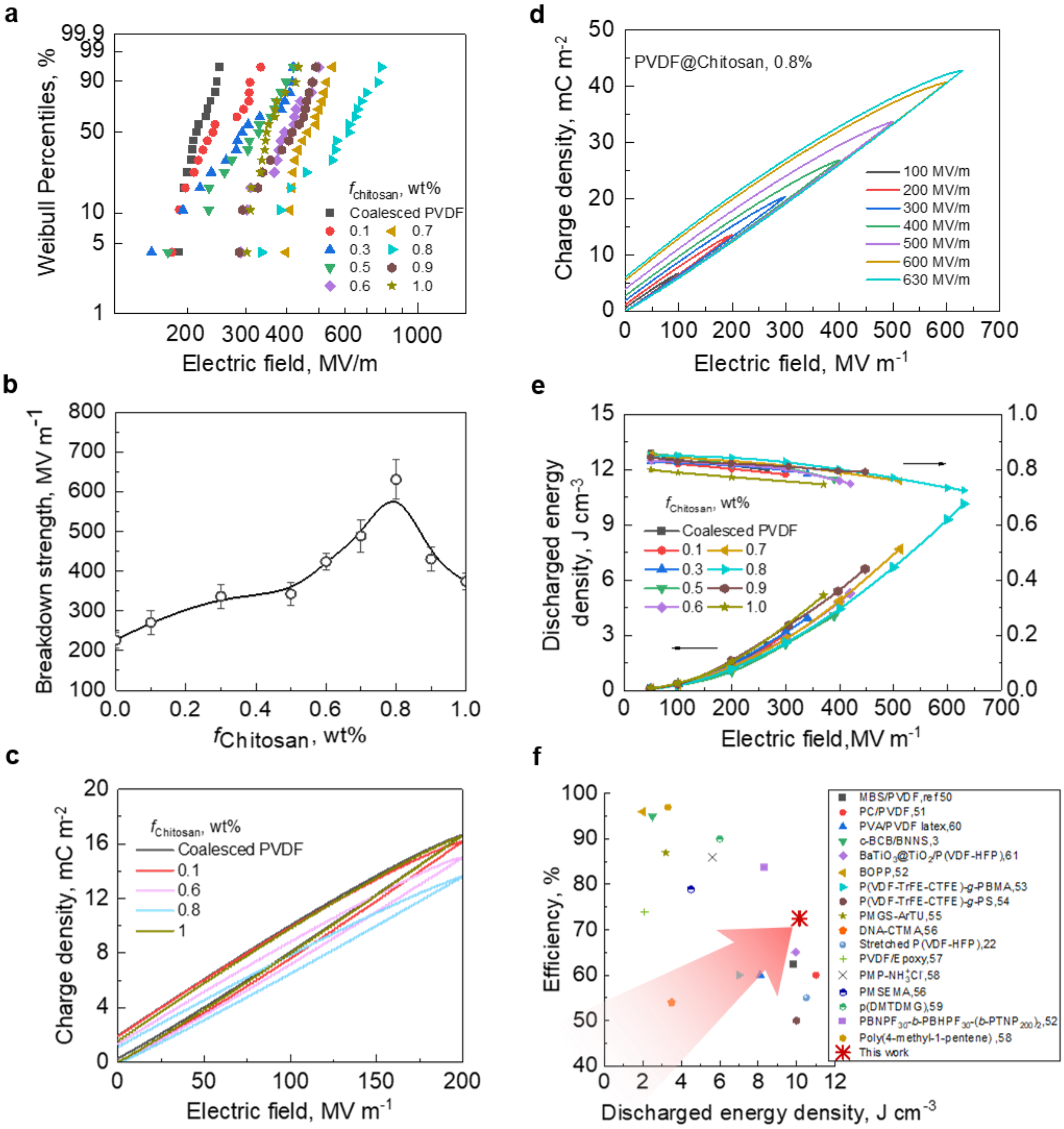

Figure 5. Breakdown strength and energy storage performances. a) Failure probability of dielectric breakdown deduced from Weibull distribution. The E_b and shape factor β are listed in Table S2 (Supporting Information). b) E_b for coalesced PVDF latex and PVDF@Chitosan films at various chitosan fractions. c) $P-E$ loops of coalesced PVDF latex and PVDF@Chitosan films at 200 MV m^{-1}. d) $P-E$ loops of PVDF@Chitosan film with f_{Chitosan} of 0.8% at different electric fields. e) Discharged energy density and charge/discharge efficiency as a function of electric field for coalesced PVDF latex and PVDF@Chitosan films. f) The comparison of discharged energy density and charge/discharge efficiency for PVDF@Chitosan film with f_{Chitosan} of 0.8% and the state-of-the-art dielectric polymers.

To evaluate power density and reliability, fast charge/discharge cycles were performed on the PVDF@Chitosan film (f_{Chitosan}=0.8%) and a commercial biaxial oriented polypropylene (BOPP) film using a typical high-speed capacitor circuit.[60] The two samples are initially charged at 200 MV m^{-1} and then discharged across a 10 kΩ load resistor in series with the sample capacitor (Figure 6a). The discharged energy density is plotted as a function of time, where the discharge time is defined as the time required to achieve 95% of the final discharged energy. The PVDF@Chitosan film liberates a stored energy of 1.148 J cm^{-3} at a rate of 1.248 μs, while the BOPP releases a stored energy of 0.299 J cm^{-3} at a rate of 1.168 μs (Figure 6b). Accordingly, the PVDF@Chitosan film exhibits a higher power density (0.92 MW cm^{-3}) as compared to 0.26 MW cm^{-3} of BOPP. Moreover, the energy density of the PVDF@Chitosan films remains constant without degradation over continuous 7610 cycles of charge/discharge (Figure 6c). In addition, the leakage current is another essential characteristic for practical applications. We performed the *P-E* loop test at a constant electric field and recorded the leakage current (Figure 6d). The leakage current density is suppressed by one order of magnitude at charge neutralization, from 2×10^{-5} A cm^{-2} (f_{Chitosan} =0) to 10^{-6} A cm^{-2} (f_{Chitosan}=0.8%) at the electric field of 100 MV m^{-1}, reaching the lowest level (highest resistivity). Such low leakage current can rival most of the recently reported high-energy dielectric materials.[2, 12, 13, 29] The great improvement of the resistivity should be ascribed to the suppression of mobile charges by the charge neutralization at the critical mass ratio (0.8 wt%) in the PVDF@Chitosan hybrid system. Combining all the merits, the charge-neutralized PVDF@Chitosan complex film shows great potential for practical dielectric energy storage applications.

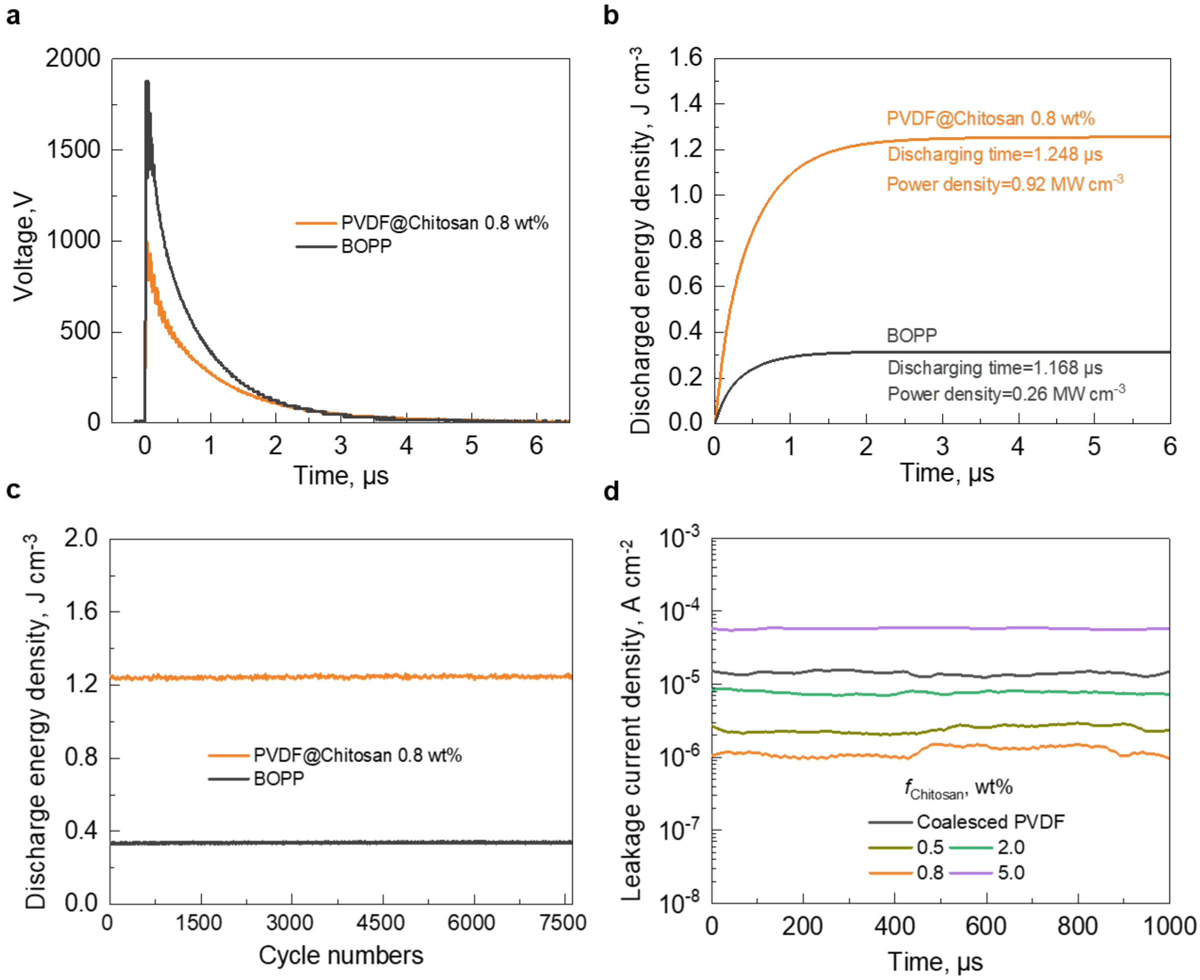

Figure 6. Charge/discharge performances. a) The voltage, and b) discharged energy density as a function of time during a charge/discharge cycle. c) Cyclic charge/discharge performances of the PVDF@Chitosan film at f_{Chitosan} of 0.8% and the BOPP film in response to a charging electric field of 200 MV m^{-1}. d) The leakage currents at a constant electric field of 100 MV m^{-1} for PVDF@Chitosan films at different f_{Chitosan}.

Furthermore, we experimentally extended the concept validated in the PVDF latex system to polystyrene (PS) latex and aqueous bentonite suspensions (Supplementary Information), which are stabilized by negative charges and represent organic and inorganic colloids respectively. Two waterborne colloidal films, PS@Chitosan and Bentonite@Chitosan, are prepared by charge neutralization at chitosan fractions of 1.1 wt% and 10 wt% respectively. At the isoelectric point, the PS@Chitosan film exhibits an E_b of 320 MV m^{-1} and an energy density of 1.4 J cm^{-3}, which show improvements of 28% and 180% over the pure PS latex films, respectively (Figure S9, Supporting Information). In addition, the resulting Bentonite@Chitosan/PVA film show the maximum energy density of 5.6 J cm^{-3} at 388 MV m^{-1} (Figure S10, Supporting Information). In contrast, the chitosan-free Bentonite/PVA composite loses the capability of energy storage beyond an electric field of 160 MV m^{-1} due to the presence of massive mobile charges in the film.

3. Conclusion

We proposed a charge neutralization strategy to substantially enhance the breakdown field and reduce the hysteretic losses of waterborne dielectrics created by using colloids as building blocks. A high energy density of 10.1 J cm^{-3} and an efficiency of 72% were achieved at 630 MV m^{-1} in charge-neutralized PVDF latex film. The finding is generic and validated in other dielectric materials manufactured from dispersions of polystyrene latex and aqueous bentonite suspension, opening thereby a widely applicable paradigm for the realization of waterborne high-energy dielectric materials.

4. Experimental Section

Materials: PVDF latex was supplied by Arkema with an initial concentration of solid content of 44 wt%, in which the ratio between the fluoropolymer and acrylic resin is 70:30. The received PVDF latex was diluted to 0.77 wt% with deionized water for use after. Chitosan pellets were purchased from Sigma-Aldrich. Protonated chitosan solution was prepared by dissolving chitosan in a 1.5 wt% acetic acid solution by magnetically stirring at 300 rpm for 4 h at room temperature, followed by heating at 120 °C for 10 minutes in an oven for sterilization, and finalized by filtration to remove insoluble impurities. A fully dissolved aqueous solution was then obtained with a final concentration of 0.66 wt% and a pH of 3.47. PS latex with a solid content of 2.6 wt% and a diameter of 0.202 μm was supplied by Polyscience Inc in Germany. These non-functionalized particles contain a slight anionic charge from sulfate ester. The received PS latex solution was diluted to 0.1 wt% for use after. Bentonite was made in EEC, Prolabo. The received bentonite powders were first washed extensively with ethanol and 1M HCl to remove excessive surfactant and ionic impurities. Subsequently, the fully washed bentonite powders were exfoliated into nanosheets by liquid phase stripping in deionized water with a tip sonication, following the established protocol.[62] An aqueous nanosheet solution was obtained at a concentration of 0.3 wt%. PVA was received from Sigma-Aldrich chemical company with a molecular weight M_w= 125 000 g mol^{-1} and a degree of hydrolysis of 99%. PVDF pellets were purchased from Sigma-Aldrich chemical company in Germany with an average molecular weight of $M_w \approx$ 530,000 g mol^{-1}. HCl was provided by Sigma-Aldrich chemical company in Germany whose assay is 37%. Ethanol was supplied by Atlantic labo. The solvent N, N-Dimethylacetamide was provided by Sigma-Aldrich.

Charge-Neutralized Colloid@Chitosan Films: To formulate charge-neutralized PVDF@Chitosan films, various amounts of protonated chitosan solution were mixed with PVDF latex by magnetic stirring at room temperature for 2 h. To precisely control the mass ratio between PVDF and chitosan, the protonated chitosan aqueous solution was added drop-by-drop into the diluted PVDF latex dispersion using a syringe. The mixture was then centrifuged. After removing the supernatant, the collected slurry was transferred onto an aluminum Petri dish. Water was then evaporated under infrared light for 60 min to obtain solid free-standing PVDF@Chitosan films. Following the same protocol, PS@Chitosan films were achieved at various chitosan fractions: 0.5

wt%, 1.1 wt%, 5 wt%, 10 wt%, and 50 wt%. While, to improve the film-forming property of bentonite nanosheets, 20 wt% PVA was added to the mixture to serve as a binder. The final solute concentration of the different aqueous mixtures was kept at 0.64 wt% by adding different amounts of deionized water. The Bentonite@Chitosan/PVA films were finally cast in an aluminum petri dish. Water was firstly evaporated at room temperature overnight and then followed by incubation at 100 °C for 20 h in a vacuum oven. Prior to the dielectric test, all the dried films were hot-pressed at 110 °C for 3 min under 40 MPa to eliminate structural defects.

Ion-Containing PVA/CH_3COONa Films: To clarify the impact of ions on the dielectric performance and energy storage density, an aqueous PVA solution was prepared according to the reported protocols.[63] CH_3COONa solution was achieved by mixing 1M NaOH and 1M CH_3COOH in 1L deionized water, followed by 4h magnetic stirring. The CH_3COONa solution was then added to the PVA solution to prepare ion-containing PVA precursors at different ion contents. Afterward, the PVA/CH_3COONa films were cast from their mixture solutions, followed by incubation procedures used for the preparation of colloid@Chitosan films.

Characterizations: The dielectric properties of the films were characterized at room temperature using an impedance analyzer (MaterialsMates 7260, Italia). The dielectric breakdown strength and $P-E$ loops were tested at room temperature in silicone oil by a PolyK ferroelectric polarization loop and dielectric breakdown test system. Fast charge and discharge experiments were performed using a capacitor charge/discharge system (PolyK Technologies). Before the characterizations, gold electrodes were sputtered on the two surfaces of each film to ensure good contact. TEM images of PVDF@Chitosan films were taken via a Hitachi H600 microscope operating at 75 kV. For TEM characterizations, the samples were ultramicrotomized into 40–60 nm thick slices using a cryo ultramicrotome (Leica UC7). The thin slices were placed on 150 mesh copper grids covered with a formvar film for observation. The morphology of the materials was also characterized by field emission gun SEM (Hitachi S4500) operating at 5 kV. The Energy-Dispersive Xray Spectroscopy spectra and the mappings were obtained on a ZEISS EVO 50 SEM equiped with an EDX EDAX detector. The electronic source was a lanthanum hexaboride tip (LaB6) and the accelerating voltage was 20 kV. The *zeta* potentials of the dispersions were recorded at 20°C using disposable cuvettes with a capillary channel and a Zetasizer Nano ZS apparatus (Malvern Instruments Ltd., Worcestershire, UK). Atomic force microscopy (AFM) images of the exfoliated bentonite nanosheets were recorded in the dry state using Tapping Mode with a scan rate of 1 Hz with a Dimension ICON (Veeco, Bruker). The samples were prepared by spin-coating diluted bentonite solutions onto a silicon wafer. The data were analyzed with Nanoscope Analysis software. The mechanical properties of the PVDF-based films were evaluated via uniaxial tensile tests on a Zwick Z2S apparatus.

Supporting Information

Supporting Information is available from the Wiley Online Library or from the author.

Acknowledgments

This research is supported by the project 3Dielectric from Agence Nationale de la Recherche (ANR-21-CE06-0001-01), and by the Thomas Jefferson Fund from the Make Our Planet Great Again Initiative of the French Presidency. This study also received financial support from the French government in the framework of the University of Bordeaux's IdEx "Investments for the

Future" program/GPR PPM. All authors thank Arkema company for the donation of PVDF materials used in this research.

Conflict of Interest

The authors declare no competing interests.

Author contributions

J. Yuan proposed and designed the project. J. Che performed the experiments. J. Che and W. Neri fabricated the sample and carried out the electrical measurements. I. Ly conducted the microstructural research, and E. Laurichesse assisted with *zeta* potential characterizations. J. Che, C. Zakri, J.-P. Chapel, P. Poulin, and J. Yuan analyzed the data. J. Che, J.-P. Chapel, P. Poulin and J. Yuan wrote and revised the manuscript. All authors discussed the results and commented on the manuscript.

Data Availability Statement

The data that support the findings of this study are available from the corresponding author upon reasonable request.

Keywords

Electrostatic complexation, PVDF latex, Chitosan, Dielectric film, Energy storage

Received: ((will be filled in by the editorial staff))
Revised: ((will be filled in by the editorial staff))
Published online: ((will be filled in by the editorial staff))

References

[1] H. Li, T. N. Yang, Y. Zhou, D. Ai, B. Yao, Y. Liu, L. Li, L. Q. Chen, Q. Wang, *Adv. Funct. Mater.* **2021**, 31, *1*, 2006739.
[2] H. Pan, F. Li, Y. Liu, Q. H. Zhang, M. Wang, S. Lan, Y. P. Zheng, J. Ma, L. Gu, Y. Shen, P.

Yu, S. J. Zhang, L. Q. Chen, Y. H. Lin, C. W. Nan, *Science* **2019**, *365*, 578.

[3] Q. Li, L. Chen, M. R. Gadinski, S. H. Zhang, G. Z. Zhang, H. Y. Li, A. Haque, L. Q. Chen, T. N. Jackson, Q. Wang, *Nature* **2015**, *523*, 576.

[4] Z.-M. Dang, J.-K. Yuan, J.-W. Zha, T. Zhou, S.-T. Li, G.-H. Hu, *Prog. Mater. Sci.* **2012**, *57*, 660.

[5] B. Chu, X. Zhou, K. Ren, B. Neese, M. Lin, Q. Wang, F. Bauer, Q. M. Zhang, *Science* **2006**, *313*, 334.

[6] P. Simon, Y. Gogotsi, *Nat. Mater.* **2008**, *7*, 845.

[7] H. Palneedi, M. Peddigari, G. T. Hwang, D. Y. Jeong, J. Ryu, *Adv. Funct. Mater.* **2018**, *28*, 1803665.

[8] Z.-M. Dang, J.-K. Yuan, S.-H. Yao, R.-J. Liao, *Adv. Mater.* **2013**, *25*, 6334.

[9] B. Xu, J. Íñiguez, L. Bellaiche, *Nat. Commun*. **2017**, 8, 15682.

[10] D. Q. Tan, *Adv. Funct. Mater.* **2020**, *30*, 1808567.

[11] H. R. Bai, K. Zhu, Z. Wang, B. Shen, J. W. Zhai, *Adv. Funct. Mater.* **2021**, *31*, 2102646.

[12] J. Kim, S. Saremi, M. Acharya, G. Velarde, E. Parsonnet, P. Donahue, A. Qualls, D. Garcia, L. W. Martin, *Science* **2020**, *369*, 81.

[13] B. Yang, Y. Zhang, H. Pan, W. Si, Q. Zhang, Z. Shen, Y. Yu, S. Lan, F. Meng, Y. Liu, H. Huang, J. He, L. Gu, S. Zhang, L.-Q. Chen, J. Zhu, C.-W. Nan, Y.-H. Lin, *Nat. Mater.* **2022**, *21*, 1074.

[14] G. Wang, Z. Lu, Y. Li, L. Li, H. Ji, A. Feteira, D. Zhou, D. Wang, S. Zhang, I. M. Reaney, *Chem. Rev*. **2021**, *121*, 6124.

[15] Z. H. Yao, Z. Song, H. Hao, Z. Y. Yu, M. H. Cao, S. J. Zhang, M. T. Lanagan, H. X. Liu, *Adv. Mater*. **2017**, *29*, 1601727.

[16] Q. Y. Zhang, X. Chen, B. Zhang, T. Zhang, W. C. Lu, Z. Chen, Z. Y. Liu, S. H. Kim, B. Donovan, R. J. Warzoha, E. D. Gomez, J. Bernholc, Q. M. Zhang, *Matter* **2021**, *4*, 2448.

[17] X. D. Wu, X. Chen, Q. M. Zhang, D. Q. Tan, *Energy Stor. Mater.* **2022**, *44*, 29.

[18] J. W. McPherson, J. Kim, A. Shanware, H. Mogul, J. Rodriguez, *IEEE Trans. Electron Devices* **2003**, *50*, 1771.

[19] X. Zhang, Y. Shen, Q. H. Zhang, L. Gu, Y. H. Hu, J. W. Du, Y. H. Lin, C. W. Nan, *Adv. Mater*. **2015**, *27*, 819.

[20] X. Huang, P. Jiang, *Adv. Mater*. **2015**, *27*, 546-554.

[21] L. L. Ren, H. Li, Z. L. Xie, D. Ai, Y. Zhou, Y. Liu, S. Y. Zhang, L. J. Yang, X. T. Zhao, Z. R. Peng, R. J. Liao, Q. Wang, *Adv. Energy Mater*. **2021**, *11*, 2101297.

[22] F. X. Guan, J. L. Pan, J. Wang, Q. Wang, L. Zhu, *Macromolecules* **2010**, *43*, 384.

[23] N. Meng, X. T. Ren, G. Santagiuliana, L. Ventura, H. Zhang, J. Y. Wu, H. X. Yan, M. J. Reece, E. Bilotti, *Nat. Commun*. **2019**, *10*, 4535.

[24] T. Zhang, X. Chen, Y. Thakur, B. Lu, Q. Y. Zhang, J. Runt, Q. M. Zhang, *Sci. Adv*. **2020**, *6*, eaax6622.

[25] J. Y. Jiang, Z. H. Shen, J. F. Qian, Z. K. Dan, M. F. Guo, Y. He, Y. H. Lin, C. W. Nan, L. Q. Chen, Y. Shen, *Nano Energy* **2019**, *62*, 220.

[26] E. Baer, L. Zhu, *Macromolecules* **2017**, *50*, 2239.

[27] Y. Jiang, X. Zhang, Z. H. Shen, X. H. Li, J. J. Yan, B. W. Li, C. W. Nan, *Adv. Funct. Mater.* **2020**, *30*, 1906112.

[28] L. Sun, Z. C. Shi, B. L. He, H. L. Wang, S. A. Liu, M. H. Huang, J. Shi, D. Dastan, H. Wang,

Adv. Funct. Mater. **2021**, *31*, 2100280.

[29] T. Wang, R. C. Peng, W. J. Peng, G. H. Dong, C. Zhou, S. Yang, Z. Y. Zhou, M. Liu, *Adv. Funct. Mater.* **2022**, *32*, 2108496.

[30] S. M. Goodman, J. Che, W. Neri, J. Yuan, A. B. Dichiara, *Energy Stor. Mater*. **2022**, *48*, 497.

[31] V. Tomer, C. A. Randall, G. Polizos, J. Kostelnick, E. Manias, *J. Appl. Phys.* **2008**, *103*, 034115.

[32] H. Tang, Y. Lin, H. A. Sodano, *Adv. Energy Mater*. **2012**, *2*, 469.

[33] Y. D. Jiang, J. Wang, S. L. Yan, Z. H. Shen, L. J. Dong, S. J. Zhang, X. Zhang, C. W. Nan, *Adv. Funct. Mater.* **2022**, *32*, 2200848.

[34] Z. H. Shen, J. J. Wang, Y. H. Lin, C. W. Nan, L. Q. Chen, Y. Shen, *Adv. Mater*. **2018**, *30*, 1704380.

[35] L. A. Renna, C. J. Boyle, T. S. Gehan, D. Venkataraman, *Macromolecules* **2015**, *48*, 6353.

[36] J. Gao, Y. S. Yang, D. Lee, S. Holdcroft, B. J. Frisken, *Macromolecules* **2006**, *39*, 8060.

[37] P. Patoka, M. Giersig, *J. Mater. Chem.* **2011**, *21*, 16783.

[38] T. S. Gehan, M. Bag, L. A. Renna, X. B. Shen, D. D. Algaier, P. M. Lahti, T. P. Russell, D. Venkataraman, *Nano Lett.* **2014**, *14*, 5238.

[39] T. Kietzke, D. Neher, K. Landfester, R. Montenegro, R. Güntner, U. Scherf, *Nat. Mater*. **2003**, *2*, 408.

[40] J. H. Choi, H. Wang, S. J. Oh, T. Paik, P. S. Jo, J. Sung, X. C. Ye, T. S. Zhao, B. T. Diroll, C. B. Murray, C. R. Kagan, *Science* **2016**, *352*, 205.

[41] R. J. Hunter, *Foundations of Colloid Science*, Vol. I, Oxford University Press Inc., New York **1986**.

[42] H. Li, M. Fauquignon, M. Haddou, C. Schatz, J.-P. Chapel, *Polymers* **2021**, *13*, 3848.

[43] V. Rao, J. Johns, *J. Appl. Polym. Sci*. **2008**, *107*, 2217.

[44] K. H. Stark, Garton, C. G., *Nature* **1955**, 176, *4495*, 1225.

[45] J.-K. Yuan, Z.-M. Dang, S.-H. Yao, J.-W. Zha, T. Zhou, S.-T. Li, J. Bai, *J. Mater. Chem.* **2010**, *20*, 2441.

[46] J.-K. Yuan, S.-H. Yao, Z.-M. Dang, A. Sylvestre, M. Genestoux, J. Bai, *J. Phys. Chem. C* **2011**, *115*, 5515.

[47] W. J. Li, Q. J. Meng, Y. S. Zheng, Z. C. Zhang, W. M. Xia, Z. Xu, *Appl. Phys. Lett*. **2010**, *96*, 192905.

[48] B. H. Fan, Z. L. Xing, F. Bedoui, J. K. Yuan, X. X. Lu, D. L. He, M. Y. Zhou, C. Zhang, Z. M. Dang, S. Weigand, J. B. Bai, *Polymer* **2020**, *190*, 122235.

[49] F. Torres-Canas, J. Yuan, I. Ly, W. Neri, A. Colin, P. Poulin, *Adv. Funct. Mater.* **2019**, *29*. 1901884.

[50] M. S. Zheng, J. W. Zha, Y. Yang, P. Han, C. H. Hu, Z. M. Dang, *Appl. Phys. Lett*. **2016**, *109*, 072902.

[51] M. Mackey, D. E. Schuele, L. Zhu, L. Flandin, M. A. Wolak, J. S. Shirk, A. Hiltner, E. Baer, *Macromolecules* **2012**, *45*, 1954.

[52] J. Chen, Y. Wang, H. Li, H. Han, X. Liao, R. Sun, X. Huang, M. Xie, *Chem. Mater*. **2018**, *30*, 1102.

[53] J. J. Li, X. Hu, G. X. Gao, S. J. Ding, H. Y. Li, L. J. Yang, Z. C. Zhang, J. *Mater. Chem. C* **2013**, *1*, 1111.

[54] F. Guan, J. Wang, L. Yang, J.-K. Tseng, K. Han, Q. Wang, L. Zhu, *Macromolecules* **2011**, *44*,

2190.
[55] G. G. Hougham, Y. Jean, Macromol. *Chem. Phys*. **2014**, *215*, 103.
[56] D. M. Joyce, N. Venkat, F. Ouchen, K. M. Singh, S. R. Smith, C. A. Grabowski, P. Terry Murray, J. G. Grote, *J. Appl. Phys*. **2014**, *115*, 114108.
[57] Y. Gao, S. Chen, B. Kong, W. Wang, Y. Cheng, *IEEE Asia Conference on Power and Electrical Engineering (ACPEE)* **2020**, 866-870. DOI: 10.1109/ACPEE48638.2020.9136477
[58] M. Zhang, L. Zhang, M. Zhu, Y. Wang, N. Li, Z. Zhang, Q. Chen, L. An, Y. Lin, C. Nan, *J. Mater. Chem. A* **2016**, *4*, 4797.
[59] G. M. Treich, S. Nasreen, A. Mannodi Kanakkithodi, R. Ma, M. Tefferi, J. Flynn, Y. Cao, R. Ramprasad, G. A. Sotzing, *ACS Appl. Mater. Interfaces* **2016**, *8*, 21270.
[60] J. Che, W. Neri, I. Ly, P. Poulin, C. Zakri, J. Yuan, *ACS Appl. Energy Mater.* **2020**, *3*, 9107.
[61] D. Kang, G. Y. Wang, Y. H. Huang, P. K. Jiang, X. Y. Huang, *ACS Appl. Mater. Interfaces* **2018**, *10*, 4077.
[62] J. D. Jacobs, H. Koerner, H. Heinz, B. L. Farmer, P. Mirau, P. H. Garrett, R. A. Vaia, *J. Phys. Chem. B* **2006**, *110*, 20143.
[63] J. Yuan, W. Neri, C. Zakri, P. Merzeau, K. Kratz, A. Lendlein, P. Poulin, *Science* **2019**, *365*, 155.

The table of contents entry and figure:

*Junjin Che, Cécile Zakri, Isabelle Ly, Wilfrid Neri, Eric Laurichesse, Jean-Paul Chapel, Philippe Poulin, Jinkai Yuan**

High-Energy-Density Waterborne Dielectrics from Polyelectrolyte-Colloid Complexes

Due to stabilizing surface charges of colloids, it has long remaind challenging to develop dielectric materials by engineering colloids in water. In this work, Che *et al.* propose a versatile approach of electrostatically complexing colloids with oppositely charged polyelectrolytes to create high-energy-density dielectrics. This strategy based on soft-chemistry processes holds great potential for environmentally friendly high-performance capacitors.

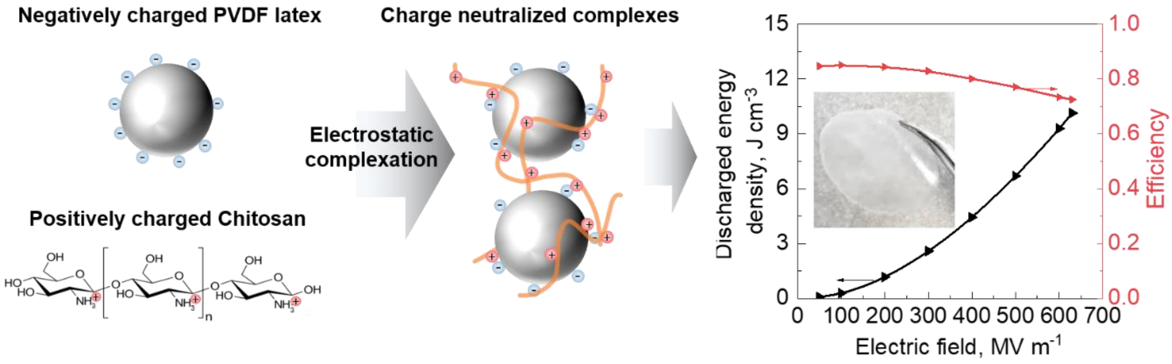

Supporting Information

High-Energy-Density Waterborne Dielectrics from Polyelectrolyte-Colloid Complexes

*Junjin Che, Cécile Zakri, Isabelle Ly, Wilfrid Neri, Eric Laurichesse, Jean-Paul Chapel, Philippe Poulin, Jinkai Yuan**

Dr. J. Che, Prof. C. Zakri, I. Ly, W. Neri, E. Laurichesse, Dr. J.-P. Chapel, Dr. P. Poulin, Dr. J. Yuan

Centre de Recherche Paul Pascal, CNRS
Université de Bordeaux
UMR 5031, 33600 Pessac, France
E-mail: jinkai.yuan@crpp.cnrs.fr (J.Y.)

Supplementary Text

ST1. Effect of Charge Carriers On the Capacitive Energy Storage
ST2. PS@Chitosan Dielectric Films
ST3. Bentonite@Chitosan/PVA Dielectric Films

Supplementary References

Figure S1-S17
Table S1-S3

Supplementary Text

ST1. Effect of Charge Carriers On the Capacitive Energy Storage

The carboxylic acid groups on PVDF nanoparticles dissociate to generate negative surface charges (COO^-) in latex solutions. Herein, the stable PVDF latex dispersion (0.72 wt%, pH=7.80) contains OH^- and Na^+ counterions. On the other hand, chitosan is protonated in acetic acid. The resultant aqueous solution (0.66 wt%, pH=3.47) contains CH_3COO^- and H^+ counterions. The complexation of cationic chitosan chains with anionic PVDF latex results in a mixture that can be considered as a hybrid dispersion consisting of CH_3COONa salts. Therefore, we examine the effects of ions on the dielectric performances and energy storage density of solid polymer composites. PVA was chosen as the matrix due to its water solubility.

The dielectric properties of PVA/CH_3COONa films were recorded as a function of frequency and shown in Figure S3 to reveal the impact of the ions on the low-field dielectric behaviors. At low CH_3COONa contents (<0.5 wt%), the apparent permittivity increases marginally over the entire frequency range. However, such a trace amount of ions can lead to a sharp rise in AC conductivity and dielectric losses of the PVA films at frequencies below 10 Hz. Such increases are associated with ion transport which usually takes time and manifests at low frequencies. Furthermore, with increasing the salt content from 1 wt% to 2 wt%, the apparent permittivity is largely boosted due to the so-called electrode polarization as a result of the formation of an electric double layer. The high loss tangent (~10) is mainly due to ionic conduction, as evidenced by a high AC conductivity (~10^{-4} S m^{-1}) that is almost independent of frequency. The introduction of ions indeed enhances the global polarization capability of the system but makes the material very lossy. Only 2 wt% of salts can turn a pure dielectric film into an ionic conductive solid electrolyte.

We also investigate the influence of the ions on the dielectric breakdown behaviors of PVA/CH_3COONa nanocomposite films. The E_b and β are calculated from a linear fitting using Weibull failure statistics (Figure S5), and the values are listed in Table S3. The E_b values of all PVA/CH_3COONa composite films are inferior to that (~500 MV m^{-1}) of the pure PVA counterpart. The breakdown strength of PVA decreases rapidly by 21% with the addition of only 0.1 wt% of CH_3COONa. As the CH_3COONa content increases up to 2.0 wt%, the breakdown continues to drop down to 182 MV m^{-1}, causing PVA to lose its capability of sustaining high voltages. In addition, the sharply decreased β values beyond 1 wt% indicate that the salts are not uniformly distributed in the films at high CH_3COONa loadings.

We further evaluated the energy storage density of different PVA samples. Based on the P-E loops at different fields until their E_b, the discharged energy density is calculated and plotted in Figure S11. Pure PVA film shows a maximum energy density of 5.2 J cm^{-3}. Despite the improvement in the overall polarization capability of the system, the discharged energy densities of ion-containing composites are inferior to that of pure PVA, because the improvement in the stored energy cannot fully compensate for the additional dissipated energy derived from the conduction losses during discharge. The higher the number of ions added to the PVA film, the lower the maximum energy density discharged from the composites. This arises from the decreased maximum field that the composite can sustain (less stored energies) as well as the increased conduction losses (more energy losses). Both trends directly give rise to a declined charge/discharge efficiency at each field with increasing salt content. Overall, it can be concluded that the presence of ions makes the materials highly lossy and dramatically deteriorates the breakdown strength and energy storage density.

ST2. PS@Chitosan Dielectric Films

Figure S12 shows the formulation process of PS@Chitosan complexes. The stably dispersed pure PS latex dispersion (0.1 wt%) and chitosan solution (0.66 wt%) exhibit *zeta* potentials of -46 mV and +89 mV, respectively. The anionic charges on PS nanoparticles arise from the dissociation of the sulfate ether groups. The PS@Chitosan hybrid particles in the mixture are subject to a net charge reversal, evidenced by the variation of *zeta* potential from negative to positive with an isoelectric point located at 1.1 wt%. At this point, the fully charge-neutralized PS@Chitosan complexes form loose aggregates, and the aggregate size reaches a maximum value of 15 μm. Different from PVDF latex, PS@Chitosan particles float on the surface of the dispersion instead of settling due to the lower density of the overall complexes (PS density~1.02 g cm^{-3}) which approaches that of water.

Figure S13 shows the frequency dependence of the low-field dielectric properties of charge-neutralized PS@Chitosan films. As with the PVDF@Chitosan systems, at the isoelectric point (1.1 wt%), the apparent permittivity is reduced from 6.5 to 2.3, a typical value of PS material.[1] In addition, the fully charge-neutralized PS@Chitosan film is the most insulating, possessing the lowest conductivity and loss tangent, which are 10^{-10} S m^{-1} and 0.016 at 100 Hz respectively.

Figure S9 shows the breakdown strength and energy storage properties of PS@Chitosan films. The E_b of pure PS latex film is found at 250 MV m^{-1}. The charge neutralization of PS nanoparticles by chitosan chains greatly suppresses the adverse effect of surface charges, leading to superior E_b. At an optimum $f_{Chitosan}$ (1.1 wt%), the E_b reaches up to a maximum value of 320 MV m^{-1}, showing an enhancement of 28% compared to pure PS latex film. Due to such high voltage tolerance, the maximum energy density of the film containing 1.1 wt% chitosan reaches up to 1.41 J cm^{-3} at 319 MV m^{-1}, which is almost three times higher than that of pure PS latex film. At this high field, the efficiency η still shows a value above 80%. The significantly improved breakdown strength and energy density of PS@Chitosan films can rival typical PS films that are free of charge carriers yet cast from toxic solvent-based solutions.[2, 3] Overall, these results indicate that our strategy could be well extended to other polymer latexes as a general approach to achieving high-energy dielectrics.

ST3. Bentonite@Chitosan/PVA Dielectric Films

We have also explored this concept in an inorganic colloidal system. Bentonite is chosen because it exists largely in the natural world and can be well dispersed in aqueous solutions. Structurally, bentonite clay is made up of two basic building blocks, i.e. aluminum octahedral sheets and silica tetrahedral sheets. In such minerals, the anionic charge of the alumina-silicate layer is neutralized by the intercalation of compensating exchangeable cations (e.g. Al^{3+}, $Ca^{2+,}$ and/or Mg^{2+}) and their coordinated water molecules. As bentonite is dispersed in an aqueous solution, it absorbs water to expand its size and releases ions to generate negative charges on surfaces and edges.

The bentonite nanosheets were first obtained by exfoliating bentonite powders in deionized water with a tip sonication. Their morphology was characterized by TEM and AFM

(Figure S14), the large bentonite nanosheet is electron transparent and very flexible with wrinkles being formed on it. An AFM image shows more details on the dimensions of achieved bentonite flakes. They have a lateral size of hundreds to thousands of nanometers and a thickness of tens of nanometers. The thickness profile of the nanosheet along the line shows a sheet dimension of ~1000 nm and an average thickness of ~10 nm. The size distribution was detected by a Zetameter with the laser diffusion method, showing a mean apparent particle diameter of 950 nm, which is consistent with the AFM measurement.

The charge states of bentonite nanosheets were examined at different f_{Chitosan} by measuring the *zeta* potential and the colloid size in the mixed dispersions. As shown in Figure S15, pure bentonite nanosheet dispersion (0.3 wt%, pH=6.6) presents a *zeta* potential of -31 mV, demonstrating the presence of negative charges on nanosheets. As adding protonated chitosan chains into bentonite dispersion, the negative *zeta* potential decreases in absolute value due to the progressive charge compensation until the isoelectric point is reached at 10 wt%. Further increasing the chitosan content, the *zeta* potential turns to be positive and increases gradually. At the isoelectric point, the size of Bentonite@Chitosan hybrid particles reaches the maximum value of 3 μm, promoting the formation of charge-neutralized loose assemblies.

Intriguingly, the isoelectric point is reached in an acid solution (10 wt%, pH=5.24) and not at a neutral pH as in the case of PVDF and PS, and the corresponding f_{Chitosan} is one order of magnitude higher than those of PVDF and PS latex. The bentonite system is indeed different from latex particles, whose negative charges are induced by the dissociation of weak acid or ether sulfate groups, which is pH dependent. The faces of the bentonite nanosheet are also negatively charged yet due to the release of the exchangeable counterions and therefore independent of pH, as evidenced by *zeta* potential measurements at varying pH from 5 to 9.5 (Figure S15c). In this system, there are no acid-based interactions, as in the case of polymer latexes, between primary amines (chitosan) and either carboxylic or ether sulfate groups causing a variation of pH with f_{Chitosan}. This mechanism allows for the formation of stable bentonite suspensions within a wide range of pH values. In this case, there is almost no pH change during complexation. More protonated chitosan groups are then needed to neutralize the surface charge of the bentonite nanosheets, requiring then a much higher f_{Chitosan}.

Bentonite and chitosan complexes are charge neutral at f_{Chitosan} of 10%. It is interesting to process them into macroscopic films for dielectric applications. To meet this end, we added 20 wt% PVA as a binder to make uniform and defect-free composite films. Figure S16 compares the morphologies of Bentonite/PVA composites with and without the decoration of chitosan chains. Intriguingly, the bentonite nanosheets tend to be stacked layer-by-layer and separated by the PVA matrix in between. This arrangement is promoted by a significant confinement effect on the orientation of anisotropic nanoparticles with large aspect ratios. The addition of chitosan does not change the layered stacking patterns but the interfaces with PVA become blurry, indicating that chitosan improves the film uniformity together with PVA.

Figure S17 shows the dielectric properties of Bentonite@Chitosan/PVA films. The apparent permittivity of Bentonite/PVA is strongly dependent on the frequency below 10^3 Hz, indicating a significant electrode polarization due to the presence of surface charges on nanosheets. These surface charges form conductive paths and induce a high AC conductivity and dielectric loss. However, at the isoelectric point (10 wt%), the apparent dielectric constant decreases from 14.3 to 11.7, and the corresponding film shows the lowest conductivity and loss tangent in the entire frequency range.

Similar to the polymer latex systems, at the isoelectric point, the E_b reaches the maximum value of 362 MV m^{-1}, showing an enhancement of 15.3% compared to that (314 MV m^{-1}) of Bentonite/PVA films (Figure S10). Though the E_b of Bentonite/PVA film is high, the film loses its energy storage capability above 160 MV m^{-1} due to the existence of massive charge carriers. A maximum energy density of only 0.226 J cm^{-3} is achieved at 100 MV m^{-1}. However, the energy density of the composite was largely improved by coating bentonite with chitosan. The optimum value achieved at f_{Chitosan} of 10% reaches 5.7 J cm^{-3} at 388 MV m^{-1}, which is 21 times higher than that of the Bentonite/PVA film. In addition, the η is greatly improved by the presence of chitosan. At a field of 100 MV m^{-1}, the η of composite with chitosan is about 85.4%, which is much higher than that (23.2%) of its counterpart without chitosan. The efficiency still maintains 49.3% at the maximum field of 388 MV m^{-1}. The significantly improved energy storage performances in bentonite films further suggest that the proposed concept is also validated in inorganic colloid systems. This widely applicable strategy thereby opens a generic route towards waterborne high-energy dielectrics.

Supplementary References

[1] L. Zhang, S. Chen, S. Yuan, D. R. Wang, P. H. Hu, Z. M. Dang, *Appl. Phys. Lett*. **2014**, 105, 052905 (2014).

[2] C. A. Grabowski, S. P. Fillery, N. M. Westing, C. Z. Chi, J. S. Meth, M. F. Durstock, R. A. Vaia, *ACS Appl. Mater. Interfaces* **2013**, 5, 5486.

[3] Z. W. Bao, C. M. Hou, Z. H. Shen, H. Y. Sun, G. Q. Zhang, Z. Luo, Z. Z. Dai, C. M. Wang, X. W. Chen, L. B. Li, Y. W. Yin, Y. Shen, X. G. Li, *Adv. Mater.* **2020**, 32, 1907227.

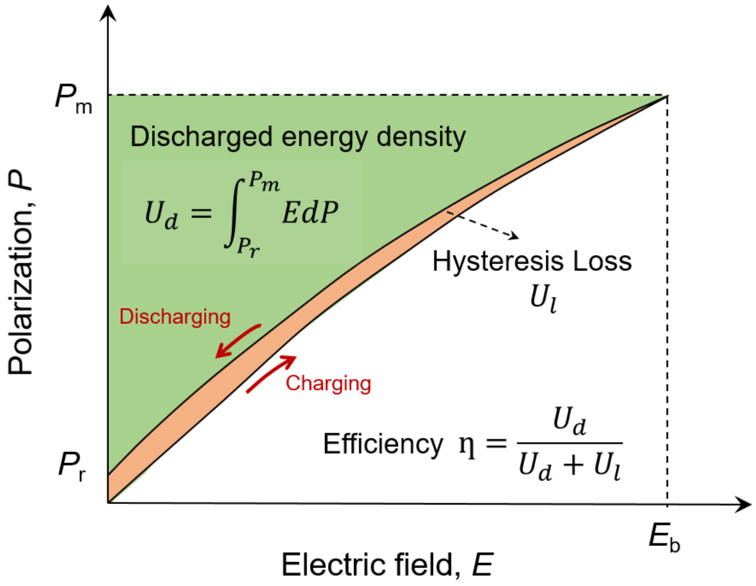

Figure S1. Energy storage in dielectric materials. Dielectric materials store energy via electric displacement in response to an external electric field. The maximum polarization P_m is achieved as the electric field approaches the breakdown strength, E_b. In the discharging process, because of the existence of hysteresis losses, only a portion of the polarization (energy) can be released, leading to a remnant polarization, P_r. The discharged energy density is represented by the green area and calculated as $U_d = \int_{P_r}^{P_m} EdP$. The yellow area represents the energy losses due to hysteretic polarization switching or leakage. The energy storage efficiency η is calculated by $\eta = U_d / (U_d + U_l)$.

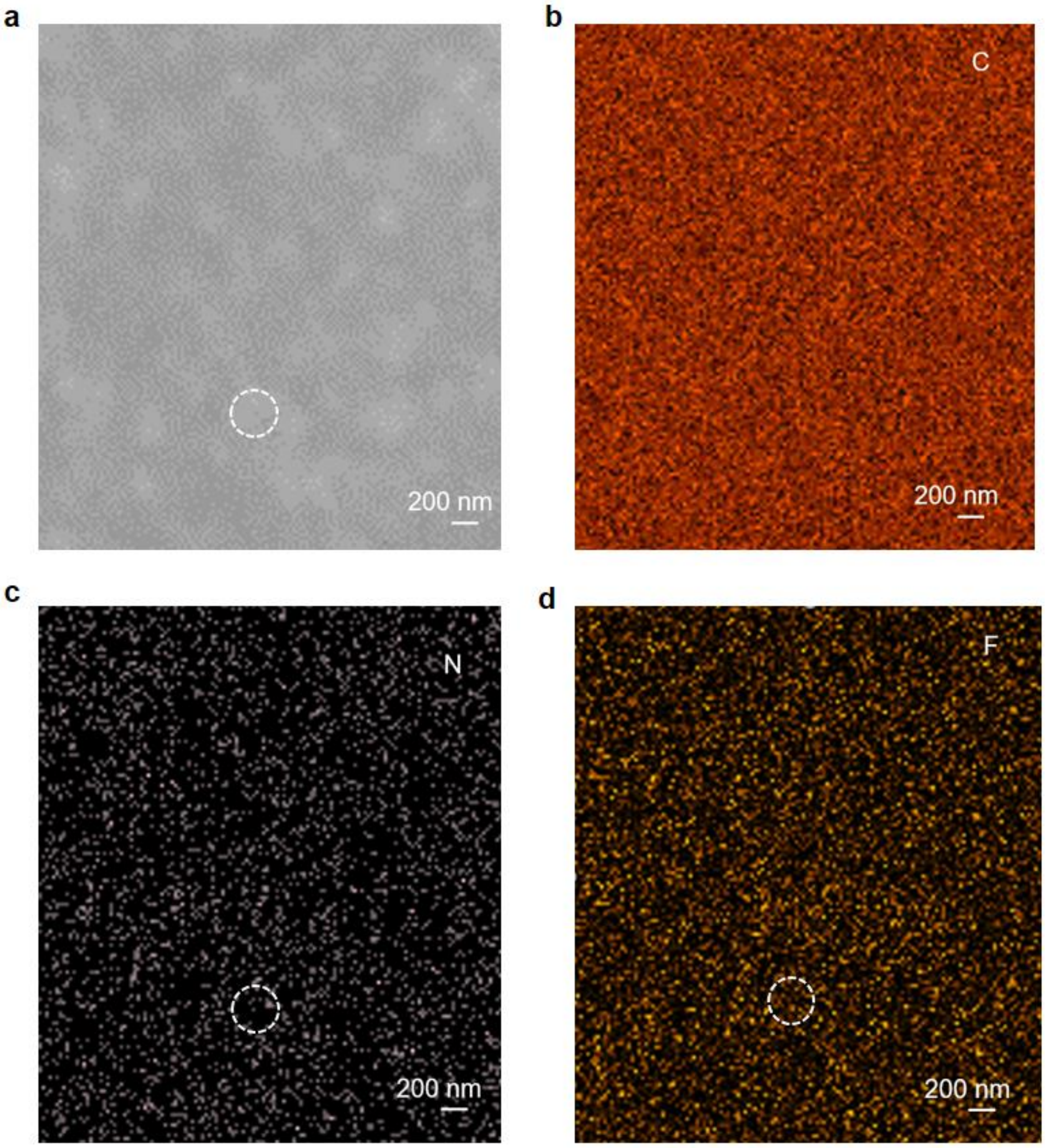

Figure S2. a) SEM image of PVDF@Chitosan and corresponding element maps of b) C, c) N, d) F, respectively. The signal of element C exhibits a uniform intensity in the entire observed region. While the signals of element F of PVDF and element N of Chitosan show segregated distributions, confirming the non-coalesced structure of PVDF latex particles. Circle area highlights a location of an individual PVDF particle, which shows a high intensity of F element. While surrounding this PVDF particle, a high intensity of N element presents.

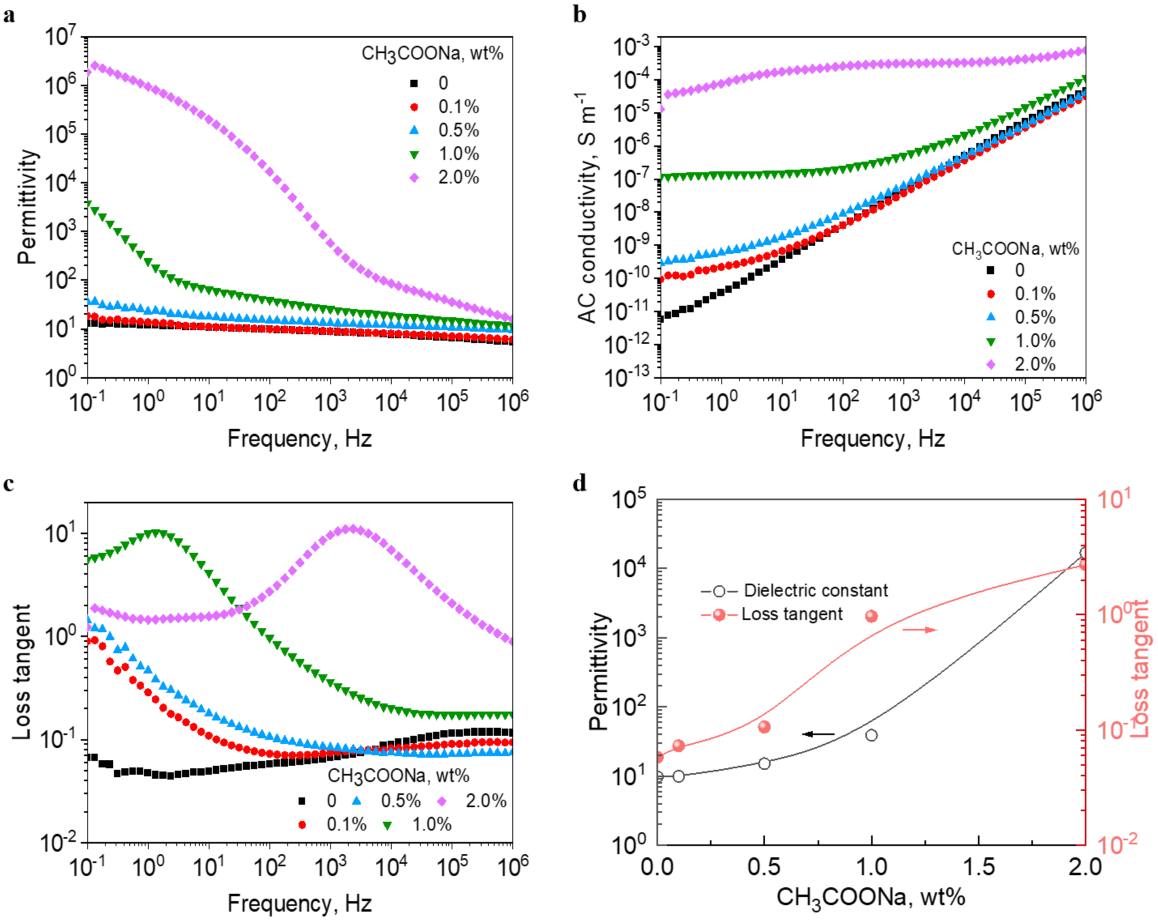

Figure S3. Dielectric performances of pure PVA and PVA/CH_3COONa films. a) Permittivity, b) AC conductivity, c) loss tangent of PVA/CH_3COONa films as a function of frequency and CH_3COONa content at room temperature. d) Dielectric constant and loss tangent at 100 Hz vary with CH_3COONa loading.

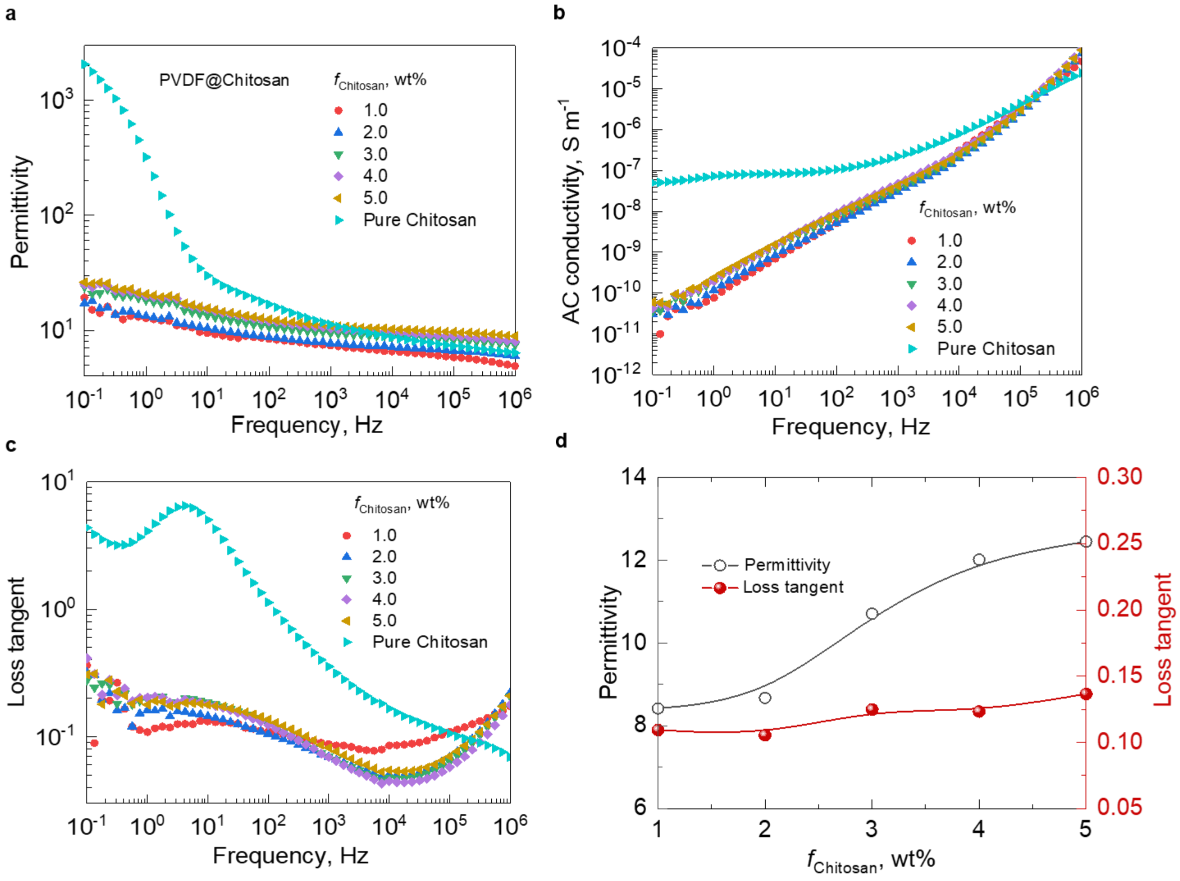

Figure S4. Dielectric properties of pure chitosan and PVDF@Chitosan films. The frequency dependence of a) permittivity, b) AC conductivity, and c) loss tangent of PVDF@Chitosan composite films with f_{Chitosan} ranging from 1 wt% to 5 wt%. d) The variation of permittivity and loss tangent at 100 Hz as a function of chitosan fraction.

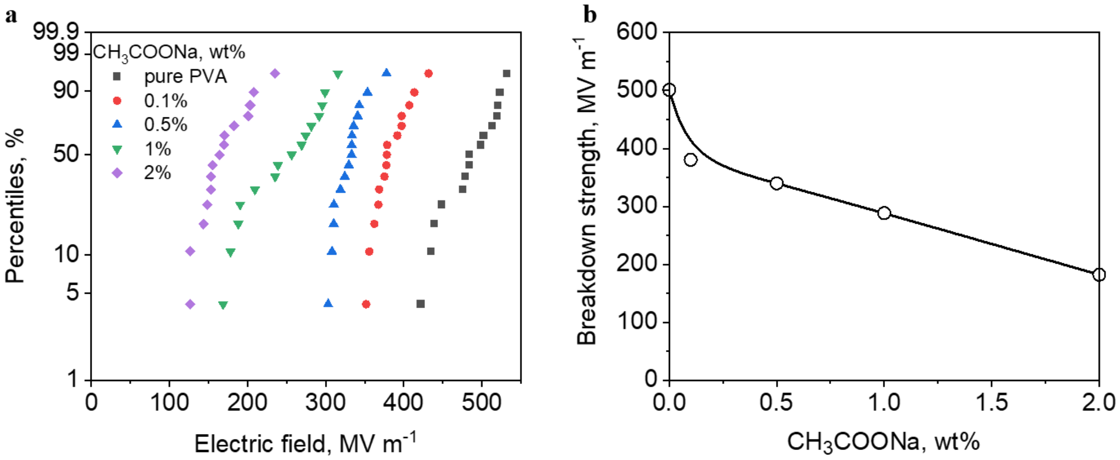

Figure S5. Breakdown strength of pure PVA and PVA/CH_3COONa composite films. a) Weibull distribution of the breakdown electric filed for neat PVA, and their composites at various CH_3COONa loadings. b) The evolution of breakdown strength as a function of CH_3COONa content.

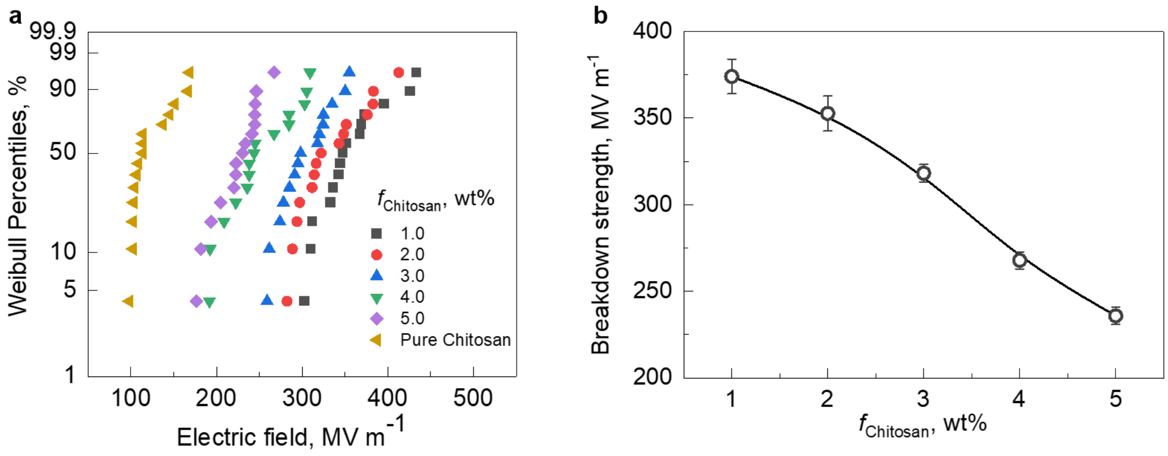

Figure S6. Dielectric breakdown behaviors of pure chitosan film and PVDF@Chitosan films with elevated f_{Chitosan}. a) Weibull distribution analysis of the breakdown field of the film Failure probability of dielectric breakdown deduced from. b) Variation of E_b for PVDF@Chitosan films with chitosan fractions.

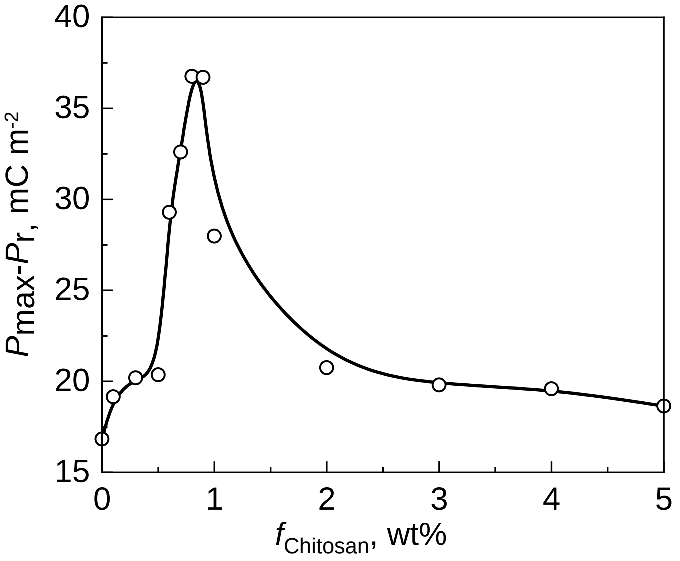

Figure S7. The variation of polarization (P_{max} - P_r) for each PVDF@Chitosan film at fields up to their breakdown strength.

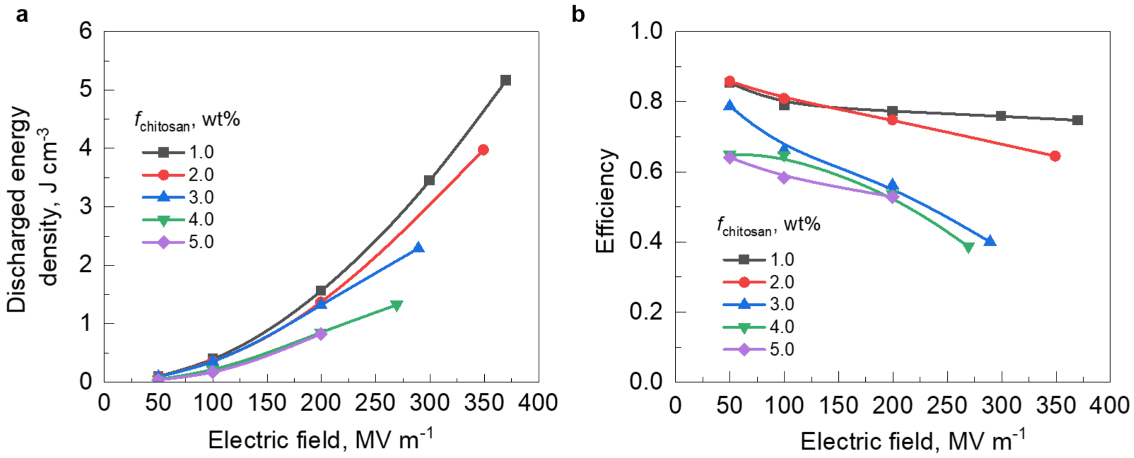

Figure S8. Energy storage properties of PVDF@Chitosan films. a) Discharged energy density, and b) charge/discharge efficiency as a function of electric field for PVDF@Chitosan nanocomposite films with excess chitosan fraction ranging from 1 wt% to 5 wt%.

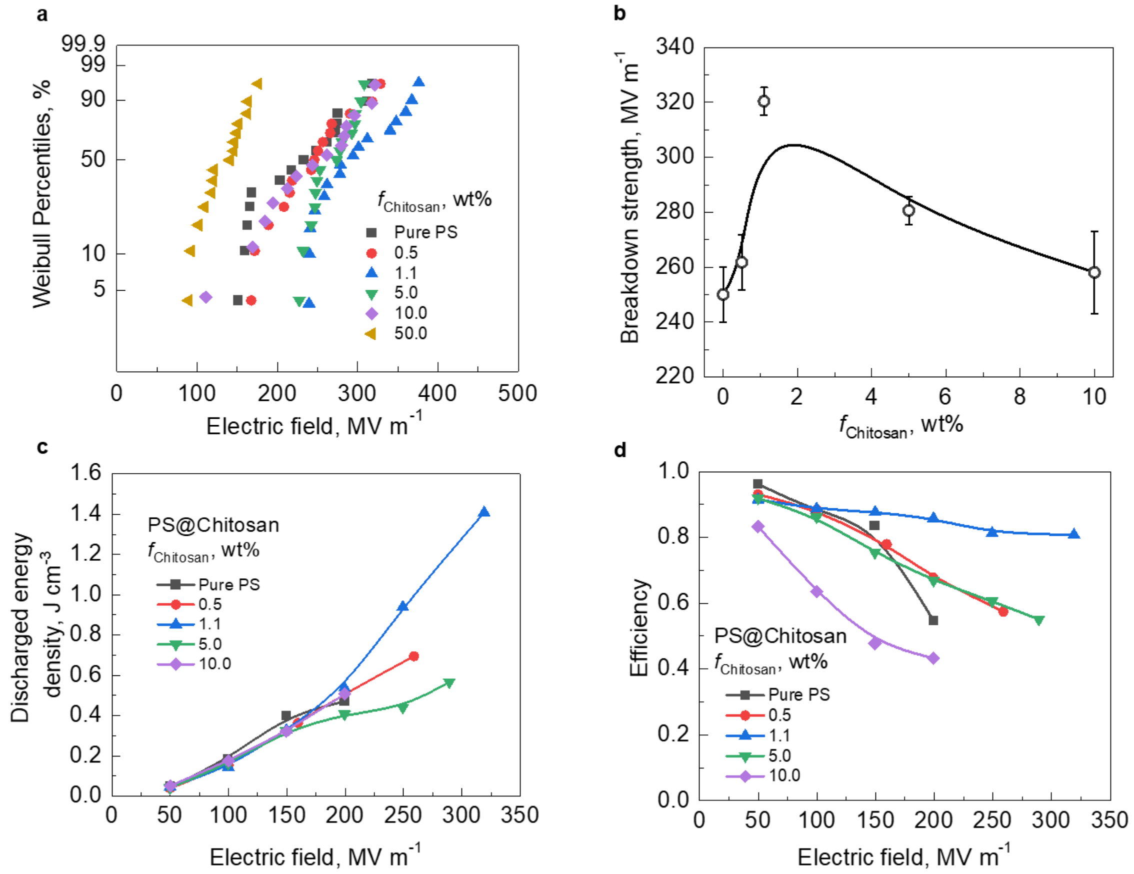

Figure S9. Energy storage properties of PS latex films. a) Failure probability of dielectric breakdown deduced from Weibull distribution for neat PS and PS@Chitosan films at various chitosan fractions. b) Evolution of breakdown strength as a function of chitosan dosage. c) Discharged energy density for pure PS and PS@Chitosan nanocomposite films. d) Charge/discharge efficiency as a function of electric field for neat PS and PS@Chitosan nanocomposite films.

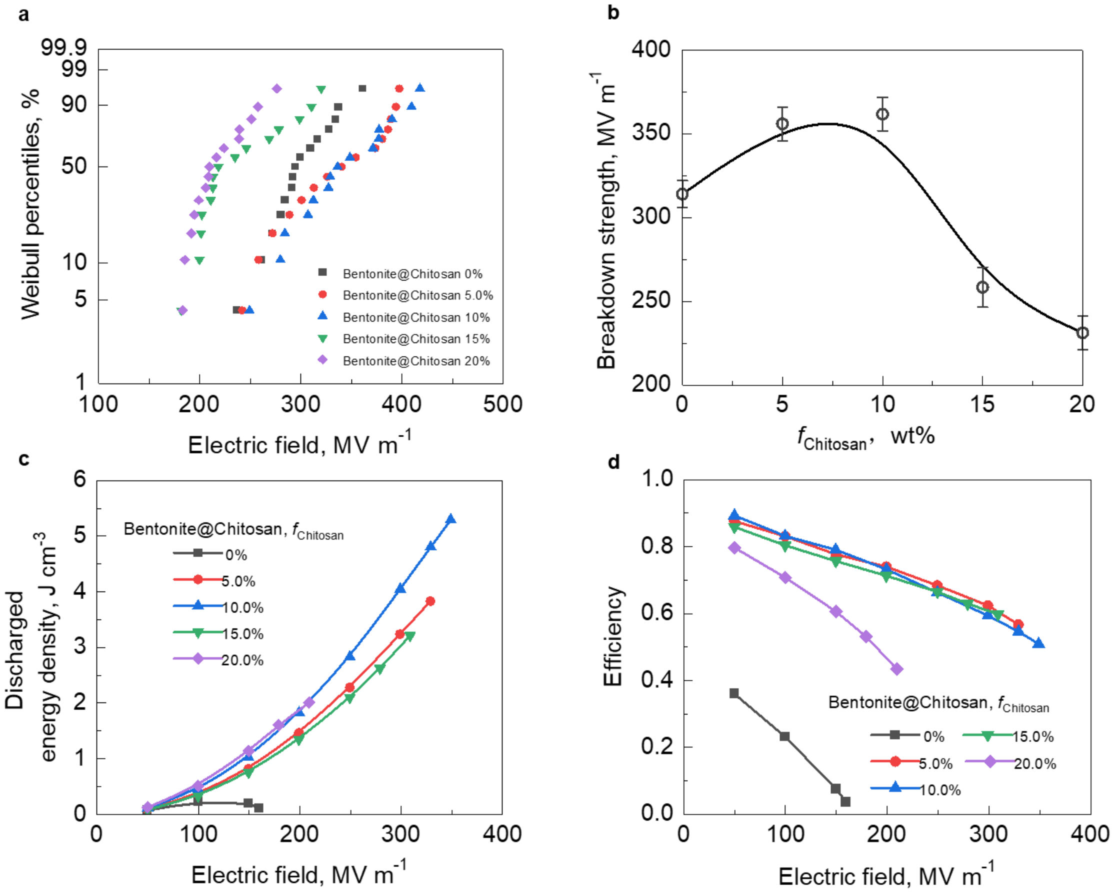

Figure S10. Energy storage performances of Bentonite@Chitosan/PVA films. a) Weibull distribution analysis of the breakdown field of the films. b) Evolution of the breakdown strength as a function of $f_{Chitosan}$. c) Field-dependent discharged energy density. d) Charge/discharge efficiency as a function of electric field for Bentonite@Chitosan/PVA films with various chitosan fractions. For each sample, the PVA content was kept at 20 wt%.

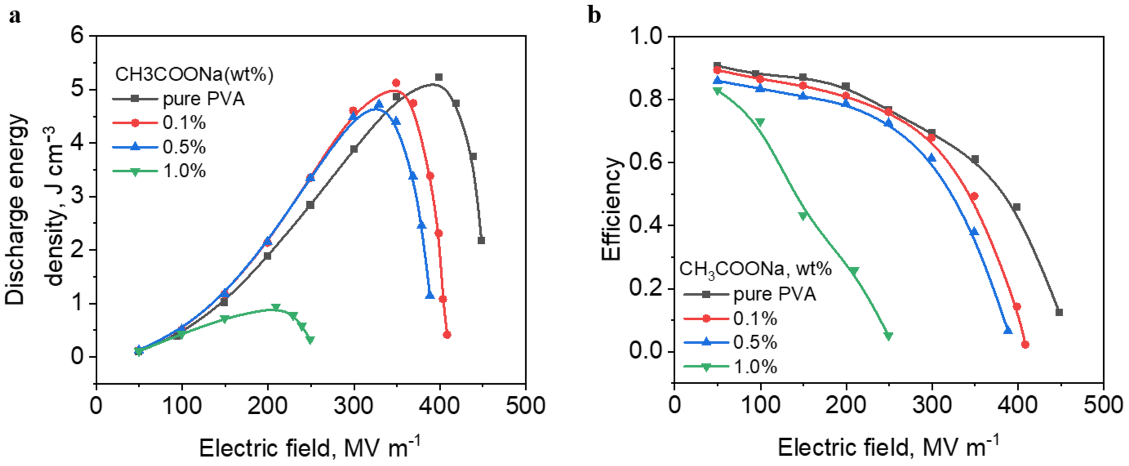

Figure S11. Energy storage properties of pure PVA and PVA/CH_3COONa nanocomposite films. a) The maximum discharged energy density, and b) The charge/discharge efficiency as a function of the electric field.

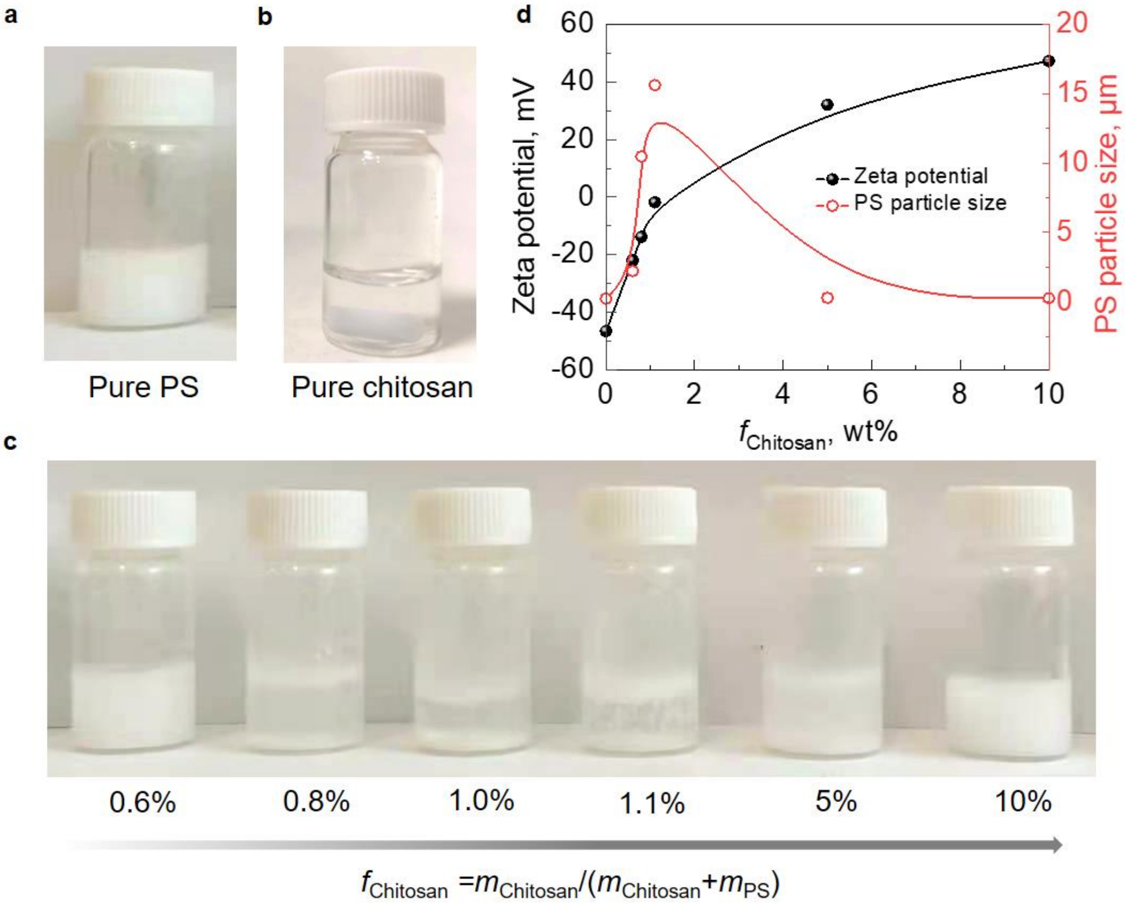

Figure S12. Formulation of PS@Chitosan complexes. Photographs of a) pure PS latex dispersion, b) pure chitosan aqueous solution, and c) the mixture of PS latex and chitosan dispersion at different fractions of chitosan. d) *Zeta* potential of the mixtures and particle size of the PS@Chitosan hybrid.

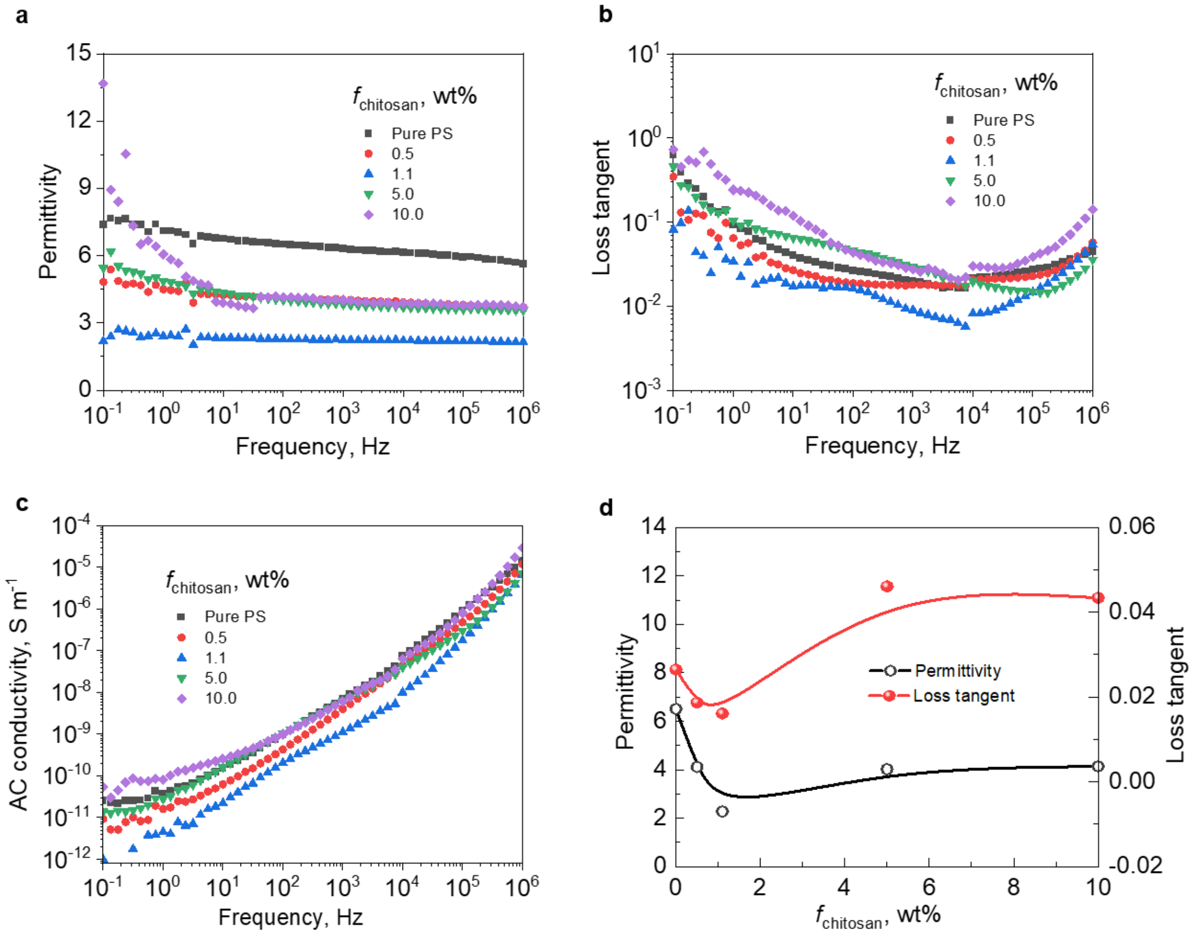

Figure S13. Dielectric performances of PS@Chitosan films. a) Permittivity, b) Loss tangent, and c) AC conductivity of PS@chitosan films as a function of frequency at room temperature. d) The plot of dielectric constant and loss tangent at 100 Hz as a function of dosage of protonated chitosan.

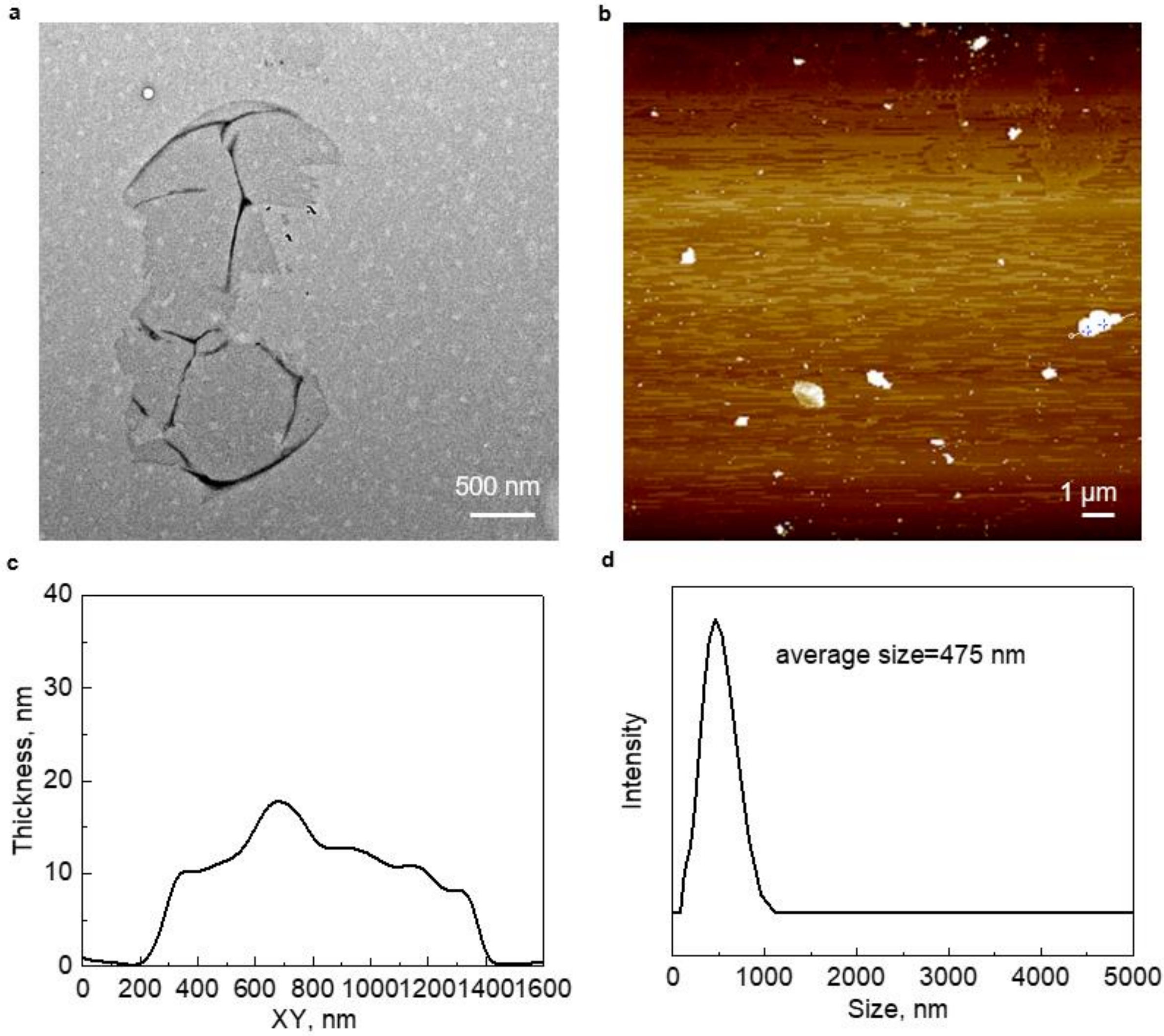

Figure S14. Characterizations of exfoliated bentonite nanosheets. a) The TEM image of bentonite nanosheet. b) AFM image of several bentonite nanosheets. c) The thickness profile along the line in b). d) The radius size distribution of exfoliated bentonite nanosheets detected by zetameter.

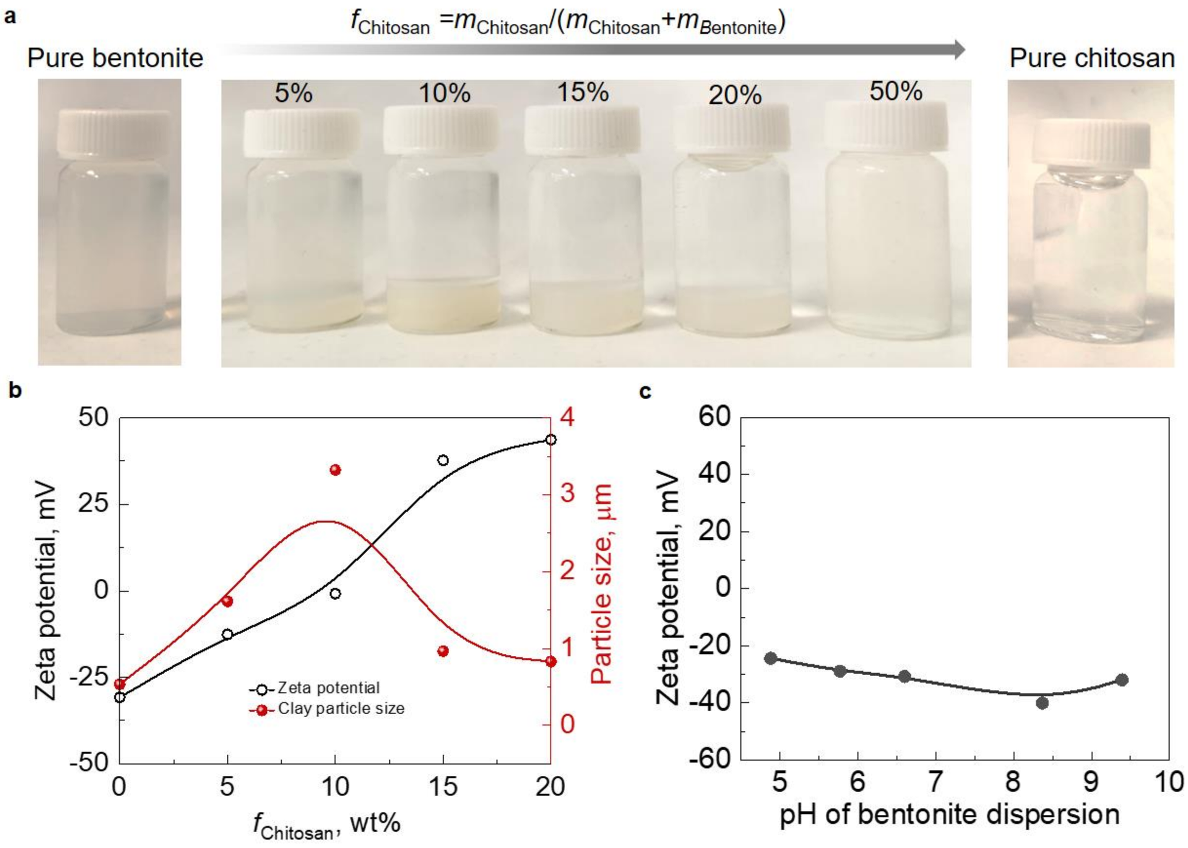

Figure S15. a) Photographs of aqueous bentonite nanosheet solution, chitosan solution, and their mixture dispersions at different mass ratios. b) *Zeta* potential of dispersions and the size of Bentonite@Chitosan hybrid particles. c) *Zeta* potential as a function of pH of bentonite nanosheet dispersions. The pH is tuned by adding CH_3COOH or NaOH to reach lower or higher values respectively.

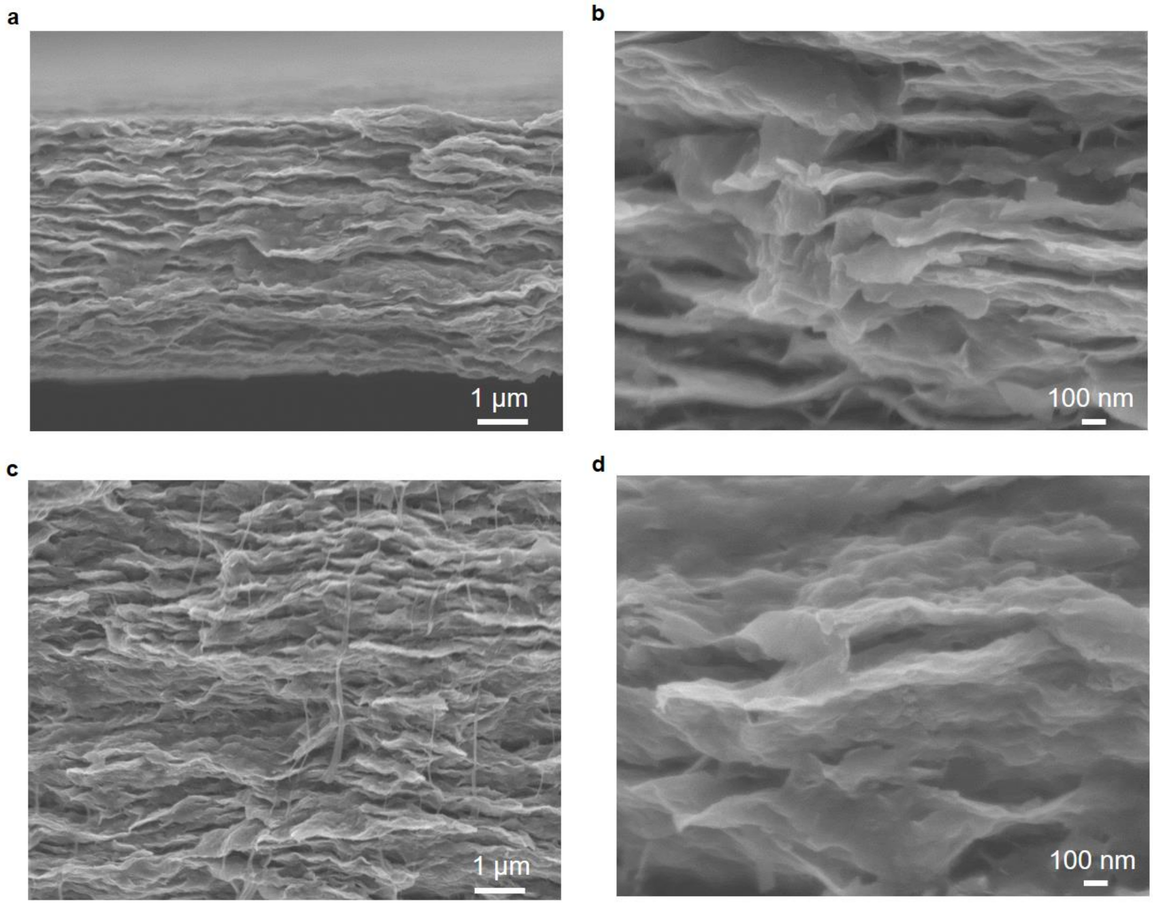

Figure S16. Cross-sectional SEM images for a,b) Bentonite/PVA, c,d) Bentonite@Chitosan/PVA (f_{Chitosan}=10 wt%) films. In each case, PVA accounts for 20 wt% of the composites.

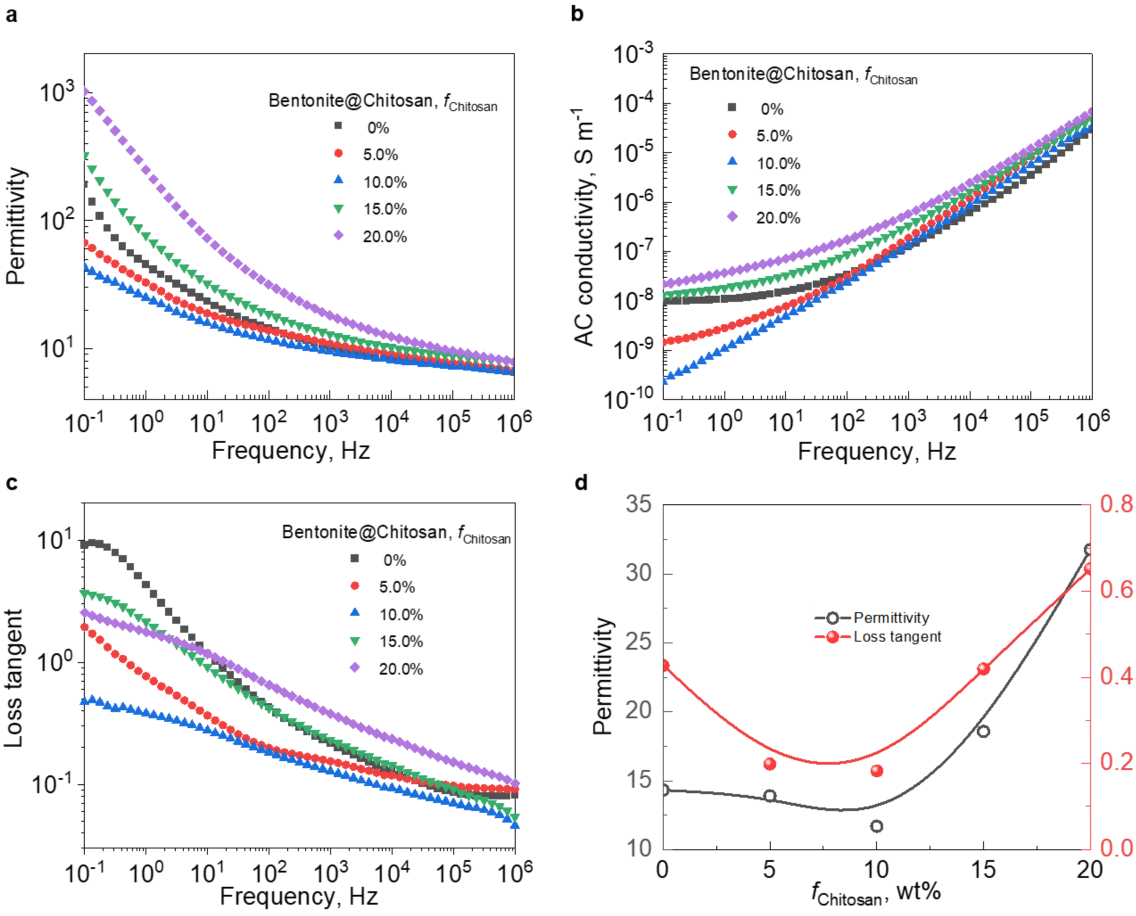

Figure S17. Low-field dielectric performances of Bentonite@Chitosan/PVA films. a) Permittivity, b) AC conductivity, c) Loss tangent of Bentonite@Chitosan/PVA films as a function of frequency at room temperature. d) Dielectric constant and loss tangent at 100 Hz varies with f_{Chitosan}. Each composite sample contains 20 wt% PVA.

Table S1. The content of each component, *zeta* potential, hybrid particle size, and pH of prepared dispersions.

Solutions	**Chitosan solution (mg)**	**PVDF latex solution (g)**	**H_2O (g)**	**PVDF content (wt %)**	**Zeta potential (mV)**	**Particle size (nm)**	**pH**
100%PVDF	0.0	7.0	0.4861	0.72	-45.9	163	7.80
99.9%PVDF/0.1%Chitosan	8.2	7.0	0.4779	0.72	-44.5	230	7.71
99.7%PVDF/0.3%Chitosan	24.6	7.0	0.4615	0.72	-43.7	505	7.68
99.6%PVDF/0.4%Chitosan	32.8	7.0	0.4533	0.72	-37.4	3207	7.66
99.5%PVDF/0.5%Chitosan	41.0	7.0	0.4451	0.72	-33.7	3674	7.62
99.4%PVDF/0.6%Chitosan	49.3	7.0	0.4368	0.72	-30.2	3734	7.47
99.3%PVDF/0.7%Chitosan	57.6	7.0	0.4285	0.72	-19.8	4857	7.3
99.2%PVDF/0.8%Chitosan	65.9	7.0	0.4203	0.72	-7.9	6486	7.02
99.1%PVDF/0.9%Chitosan	74.2	7.0	0.4119	0.72	26.6	3759	6.16
99%PVDF/1%Chitosan	82.5	7.0	0.4036	0.72	29.2	898	5.12
98%PVDF/2%Chitosan	166.7	7.0	0.3194	0.72	37.4	565	4.71
97%PVDF/3%Chitosan	252.6	7.0	0.2335	0.72	42.0	444	4.59
96%PVDF/4%Chitosan	340.3	7.0	0.1458	0.72	48.1	496	4.53
95%PVDF/5%Chitosan	429.8	7.0	0.0563	0.72	49.9	434	4.51
100% Chitosan	5000	0	0	0	89.0	n/a	3.47

Table S2. E_b and β of coalesced PVDF latex, chitosan, and the PVDF@Chitosan films at various chitosan fractions.

Chitosan content f_{Chitosan}**, wt%**	**Breakdown strength** E_b**, MV m**$^{-1}$	**Shape factor** β
Pure PVDF	226.34	12.04
0.1	270.92	5.72
0.3	336.50	4.29
0.5	342.77	5.61
0.6	423.84	7.48
0.7	488.40	10.82
0.8	630.42	5.45
0.9	430.40	7.66
1.0	373.97	9.43
2.0	352.63	9.05
3.0	318.17	11.40
4.0	267.84	7.46
5.0	235.88	10.96
Pure Chitosan	132.50	5.29

Table S3. E_b and β of pure PVA and their composites at various CH_3COONa contents

CH_3COONa, wt%	**E_b, MV m^{-1}**	**β**
0	500.37	17.66
0.1	394.20	17.28
0.5	339.65	16.12
1	265.45	6.29
2	182.23	5.84